J|A|C|S ARTICLES

Published on Web 05/21/2009

Tuning Charge Transfer Energetics in Reaction Center Mimics via T_h-Functionalization of Fullerenes

Fabian Spänig,[†] Christian Kovacs,[‡] Frank Hauke,[‡] Kei Ohkubo,[§] Shunichi Fukuzumi,*[,§] Dirk M. Guldi,*[,†] and Andreas Hirsch*[,‡]

Department of Chemistry and Pharmacy and Interdisciplinary Center of Molecular Materials (ICMM), Friedrich-Alexander Universität Erlangen Nürnberg, Egerlandstrasse 3, 91058 Erlangen, Germany, Department of Chemistry and Pharmacy and Interdisciplinary Center of Molecular Materials (ICMM), Friedrich-Alexander Universität Erlangen Nürnberg, Henkestrasse 42, 91054 Erlangen, Germany, and Department of Material and Life Science, Graduate School of Engineering, Osaka University, SORST, Japan Science and Technology Agency, Suita, Osaka 565-0871, Japan

Received February 3, 2009; E-mail: guldi@chemie.uni-erlangen.de; andreas.hirsch@chemie.uni-erlangen.de; fukuzumi@chem.eng.osaka-u.ac.jp

Abstract: We have introduced an approach of mono- and hexakis-adducts of C_{60} involving a T_h-symmetrical addition pattern, where up to 12 ferrocene or 10 ferrocene and one porphyrin units are linked flexibly to C_{60} with the objective to systematically raise the energy of the radical ion pair state. A detailed electrochemical and photophysical investigation has shed light onto charge transfer events that depend largely on (i) the functionalization pattern of C_{60}, (ii) the donor strength of the donor, (iii) the excited-state energy of the predominant chromophore, and (iv) the solvent polarity. Considering (i)−(iv), the presence of the porphyrins is key to providing sufficient driving forces for affording spatially separated radical ion pair states. An ideal scenario, that is, testing $ZnP-C_{60}-(Fc)_{10}$ (**19**) in benzonitrile and DMF, allows storing nearly 1.7 eV in a nanosecond lived radical ion pair state. In this context, the flexible linkage, powering a through space charge transfer, prevents, however, stabilization of the radical ion pair state beyond nanoseconds.

Introduction

The bacterial photosynthetic reaction center provides meaningful incentives for the optimization of charge separation processes in artificial model systems, nanometer scale structures.[1] Common to all of these systems is a relay of short-range energy/electron transfer reactions, evolving among chlorophyll and quinone moieties. Among many key parameters that govern electron transfer reactions, the reorganization energy imposes probably the most far-reaching impact. The reorganization energy (λ) is the energy required to structurally reorganize the donor, acceptor, and their solvation spheres upon electron transfer. For example, the primary electron transfer processes of photosynthesis are characterized by an extremely small reorganization energy (0.2 eV),[1] attained by the transmembrane protein environment. This aspect is central for achieving the ultrafast charge separation and retarding the energy wasting charge recombination, which is highly exergonic ($-\Delta G_{CR}^{\circ} =$ 1.2 eV).[2] It is foreseeable that the artificial photosynthetic systems that will ultimately power practical solar fuels production must be based on molecular and supramolecular assemblies. Specific requirements that such assemblies must meet include the collection of light energy, separation of charges, and transport of charges to catalytic sites, where water oxidation and CO_2 reduction will occur.[3]

Nanometer scale structures are the focus of considerable interest because they can be used to test fundamental ideas about the roles of dimensionality and confinement in materials of greatly reduced size. One cast of active nanometer scale structures that we consider are fullerenes. Since the initial discovery of fullerenes,[4] chemists and physicists worldwide have studied solid-state properties ranging from superconductivity[5] and nanostructured devices[6] to endohedral fullerene chemistry. The three-dimensional, spherical structure of fullerenes, which

[†] Friedrich-Alexander Universität Erlangen Nürnberg, Egerlandstrasse 3.
[‡] Friedrich-Alexander Universität Erlangen Nürnberg, Henkestrasse 42.
[§] Osaka University.

(1) *The Photosynthetic Reaction Center*; Deisenhofer, J., Norris, J. R., Eds.; Academic Press: New York, 1993.
(2) Guldi, D. M.; Fukuzumi, S. *Dev. Fullerene Sci.* **2002**, *4*, 237.
(3) (a) Barber, J.; Andersson, B. *Nature* **1994**, *370*, 31. (b) Armaroli, N.; Balzani, V. *Angew. Chem., Int. Ed.* **2007**, *46*, 52.
(4) (a) Kroto, H. W.; Heath, J. R.; O'Brien, S. C.; Curl, R. F.; Smalley, R. E. *Nature* **1985**, *318*, 162. (b) Curl, R. F. *Angew. Chem., Int. Ed. Engl.* **1997**, *36*, 1566. (c) Kroto, H. *Angew. Chem., Int. Ed. Engl.* **1997**, *36*, 1578. (d) Smalley, R. E. *Angew. Chem., Int. Ed. Engl.* **1997**, *36*, 1594.
(5) (a) Schön, J. H.; Kloc, C.; Haddon, R. C.; Batlogg, B. *Science* **2000**, *288*, 656. (b) Hebard, A. F.; Rosseinski, M. J.; Haddon, R. C.; Murphy, D. W.; Glarum, S. H.; Palstra, T. T. M.; Ramirez, A. P.; Kortan, A. R. *Nature* **1991**, *350*, 600. (c) Holczer, K.; Klein, O.; Huang, S.-M.; Kaner, R. B.; Fu, K.-J.; Whetten, R. L.; Diederich, F. *Science* **1991**, *252*, 1154. (d) Haddon, R. C. *Acc. Chem. Res.* **1992**, *25*, 127. (e) Rosseinsky, M. J. *J. Mater. Chem.* **1995**, *5*, 1497.
(6) (a) Fritzsche, W.; Köhler, M. *Nanotechnology: An Introduction to Nanostructuring Techniques*; Wiley-VCH: Weinheim, Germany, 2004 (b) Rao, C. *Chemistry of Nanomaterials: Synthesis, Properties and Applications*; Wiley-VCH: Weinheim, Germany, 2004. (c) Wolf, E. *Nanophysics and Nanotechnology: An Introduction to Modern Concepts in Nanoscience*; Wiley-VCH: Weinheim, Germany, 2004. (d) Cao, G. *Nanostructures and Nanomaterials: Synthesis, Properties & Applications*; Imperial College Press: London, 2004.

 10.1021/ja900675t CCC: $40.75

are composed of 12 pentagons and 20 or more hexagons with diameters starting at 7.8 Å for C_{60}, evoked a lively interest to relate their properties to conventional two-dimensional π-systems.[7] Their extraordinary electron acceptor properties, predicted theoretically and confirmed experimentally, have resulted in noteworthy advances in the areas of light-induced electron transfer chemistry[8] and solar energy conversion.[9] It is mainly the small reorganization energy, which fullerenes exhibit in electron transfer reactions, that is accountable for this noteworthy breakthrough.[10] In particular, ultrafast charge separation together with very slow charge recombination features lead to unprecedented long-lived radical ion pair states formed in high quantum efficiencies.

Original and well-established synthetic methodologies, applied to fullerenes, have produced a wide variety of novel derivatives.[11,12] In particular, such methodologies allow the chemical functionalization of fullerenes in simple or even sophisticated ways. On the basis of these methods, the synthesis of relatively complex molecular architectures, tetrads and even hexads, has been accomplished, in which the unique electrochemical and photophysical features of C_{60} have largely been preserved.[13]

The rich and extensive absorptions (i.e., $\pi-\pi^*$ transitions) seen in porphyrinoid systems, the pigments of life, hold particular promise for increased absorptive cross sections and thus an efficient use of the solar spectrum. Over the course of recent years, they have emerged as light harvesting building blocks in the construction of molecular architectures.[14] Their high electronic excitation energy, typically exceeding 2.0 eV, powers a strongly exergonic electron transfer, which subsequently intercedes the conversion between light and chemical/electrical energy. Another class of interesting electron donors are ferrocenes that are available in large quantities. Importantly, ferrocences are easily converted into reactive precursors that react readily with C_{60}.[15] So far, however, only monoadducts of C_{60} or $C_{59}N$ bearing ferrocenes have been investigated, for example, by the groups of Langa,[16] Descheneaux,[17] and ourselves.[18]

So far, the aspect to fine-tune the radical ion pair state by systematically altering the functionalization pattern of C_{60} has received little attention. This is where the current work was meant to make a significant contribution. In particular, we have introduced for the first time an approach of mono- and hexakis-adducts of C_{60} involving a T_h-symmetrical addition pattern, where up to 12 ferrocene units are linked to C_{60} including hybrid materials that contain 10 ferrocene units and one additional porphyrin. An important asset of the hexakis-adducts of C_{60} is their cathodically shifted reduction potential, relative to that of monoadducts of C_{60}, which raises the energy of the radical ion pair state significantly. Considering the small reorganization energies of C_{60} in charge transfer reactions, in combination with porphyrins, raising the radical ion pair state energy is expected to push the energy wasting and unwanted charge recombination deeper into the Marcus inverted region and, in turn, to slow it down. To carefully evaluate the corresponding charge transfer processes, we have also prepared a series of reference compounds lacking electron donating ferrocenes and/or porphyrins. To this end, we have taken advantage of the straightforward nucleophilic cyclopropanation chemistry of C_{60}[19−21] to attach the corresponding functional units. In this study, we have documented the energetics, charge separation, and charge recombination of hexakis-adducts of C_{60} containing a series of ferrocenes and porphyrins in comparison with those of reference compounds by electrochemical studies, fluorescence lifetime, and femotosecond laser flash photolysis measurements.

Results and Discussion

Synthesis and Structural Characterization. Nucleophilic cyclopropanation of the [6:6]-bonds with malonates emerged as one of the most suitable methods to functionalize C_{60} exohedrally.[19−21] This reaction proceeds in good yields with high selectivity and tolerates a broad range of functional groups that are linked to the two malonate termini. In addition, multiple additions of malonates to C_{60}, leading to stereochemically defined oligoadducts, have been carried out with very high regioselectivity using, for example, template mediation approaches or tether strategies.[11,22] To apply such concepts within the context of targeted multiferrocene architectures, a precursor malonate was required. This was achieved by the synthesis of the bis-ferrocene building block **3**, as shown in Scheme 1. For

(7) Haddon, R. C. *Science* **1993**, *261*, 1545.
(8) (a) Imahori, H.; Sakata, Y. *Eur. J. Org. Chem.* **1999**, 2445. (b) Martín, N.; Sànchez, L.; Llescas, B.; Pérez, I. *Chem. Rev.* **1998**, *98*, 2527. (c) Guldi, D. M. *Chem. Commun.* **2000**, 321.
(9) (a) Martín, N.; Sánchez, L.; Ángeles Herranz, M.; Illescas, B.; Guldi, D. M. *Acc. Chem. Res.* **2007**, *40*, 1015. (b) Hasobe, T.; Imahori, H.; Fukuzumi, S.; Kamat, P. V. *J. Phys. Chem. B* **2003**, *107*, 12105. (c) Hasobe, T.; Imahori, H.; Kamat, P. V.; Fukuzumi, S. *J. Am. Chem. Soc.* **2005**, *127*, 121. (d) Guldi, D. M. *J. Phys. Chem. B* **2005**, *109*, 11432.
(10) (a) Imahori, H.; Hagiwara, K.; Akiyama, T.; Aoki, M.; Taniguchi, S.; Okada, T.; Shirakawa, M.; Sakata, Y. *Chem. Phys. Lett.* **1996**, *263*, 545. (b) Fukuzumi, S.; Ohkubo, K.; Imahori, H.; Guldi, D. M. *Chem.–Eur. J.* **2003**, *9*, 1585.
(11) Hirsch, A.; Brettreich, M. *Fullerenes−Chemistry and Reaction*; Wiley-VCH: Weinheim, Germany, 2004.
(12) (a) Hirsch, A.; Vostrowsky, O. *Eur. J. Org. Chem.* **2001**, 829. (b) Vostrowsky, O.; Hirsch, A. *Chem. Rev.* **2006**, *106*, 5191.
(13) (a) Diederich, F.; Isaacs, L.; Philp, D. *Chem. Soc. Rev.* **1994**, *23*, 243. (b) Prato, M.; Maggini, M. *Acc. Chem. Res.* **1998**, *31*, 519. (c) Tasis, D.; Tagmatarchis, N.; Georgakilas, V.; Gamboz, C.; Scoranno, M.-R.; Prato, M. C. R. *Chimia* **2003**, *6*, 597. (d) Tagmatarchis, N.; Prato, M. *Synlett* **2003**, *6*, 768. (e) Diederich, F.; Gomez-Lopez, M. *Chem. Soc. Rev.* **1999**, *28*, 263. (f) Fukuzumi, S. *Org. Biomol. Chem.* **2003**, *1*, 609.
(14) (a) Kalyanasundaram, K. *Photochemistry of Polypyridine and Porphyrin Complexes*; Academic Press: London, 1997. (b) Gouterman, M.; Rentzepis, P. M.; Straub, K. D. *Porphyrins: Excited States and Dynamics*; ACS Symposium Series; American Chemical Society: Washington, DC, 1987; Vol. 321. (c) Dolphin, D. *The Porphyrins*; Academic Press: New York, 1978. (d) Kadish, K. M.; Smith, K. M.; Guilard, R. *The Porphyrin Handbook*; Academic Press: New York, 2003.
(15) (a) Guldi, D. M.; Maggini, M.; Scorrano, G.; Prato, M. *J. Am. Chem. Soc.* **1997**, *119*, 974. (b) Guldi, D. M.; Maggini, M.; Scorrano, G.; Prato, M. *Res. Chem. Intermed.* **1997**, *23*, 561.
(16) (a) Perez, L.; Garcia-Martinez, J. C.; Dez-Barra, E.; Atienzar, P.; Garcia, H.; Rodriguez-Lopez, J.; Langa, F. *Chem.–Eur. J.* **2006**, *12*, 5149. (b) Delgado, J. L.; EI-Khouly, M. E.; Araki, Y.; Gomez-Escalonilla, M. J.; de la Cruz, P.; Oswald, F.; Ito, O.; Langa, F. *Phys. Chem. Chem. Phys.* **2006**, *8*, 4104.
(17) (a) Even, M.; Heinrich, B.; Guillon, D.; Guldi, D. M.; Prato, M.; Deschenaux, R. *Chem.–Eur. J.* **2001**, *7*, 2595. (b) Carano, M.; Chuard, T.; Deschenaux, R.; Even, M.; Marcaccio, M.; Paolucci, F.; Prato, M.; Roffia, S. *J. Mater. Chem.* **2002**, *12*, 829. (c) Campidelli, S.; Vazquez, E.; Nilic, D.; Prato, M.; Barbera, J.; Guldi, D. M.; Marcaccio, M.; Paolucci, D.; Paolucci, F.; Deschenaux, R. *J. Mater. Chem.* **2004**, *14*, 1266.
(18) Hauke, F.; Hirsch, A.; Liu, S.-G.; Echegoyen, L.; Swartz, A.; Luo, C.; Guldi, D. M. *ChemPhysChem* **2002**, *3*, 195.
(19) Bingel, C. *Chem. Ber.* **1993**, *126*, 1957.
(20) Camps, X.; Hirsch, A. *J. Chem. Soc., Perkin Trans. 1* **1997**, 1595.
(21) Lamparth, I.; Maichle-Mössmer, C.; Hirsch, A. *Angew. Chem.* **1995**, *107*, 1755; *Angew. Chem., Int. Ed. Engl.* **1995**, *34*, 1607.
(22) Reuther, U.; Brandmüller, T.; Donaubauer, W.; Hampel, F.; Hirsch, A. *Chem.–Eur. J.* **2002**, *8*, 2261.

Scheme 1. Synthesis of the Malonate Building Block **3** and Mono-Adduct **4**[a]

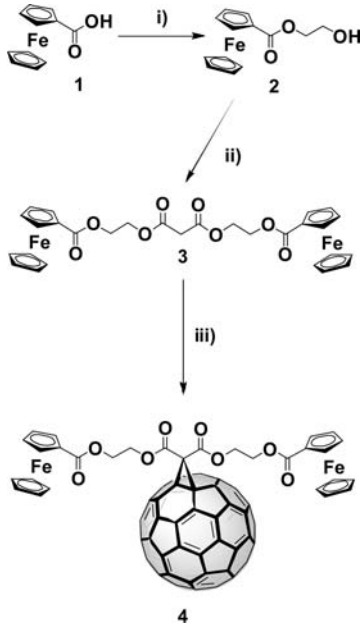

[a] (i) 0.2 equiv of DMAP, 1.0 equiv of DCC, 1.1 equiv of ethylene glycol, CH_2Cl_2, 0 °C to room temperature, 12 h, 92.2%; (ii) 1.0 equiv of pyridine, 0.5 equiv of malonyl dichloride, CH_2Cl_2, 0 °C to room temperature, 2 h, 68.8%; (iii) 2.0 equiv of C_{60}, 1.0 equiv of CBr_4, 2.0 equiv of DBU, toluene, room temperature, 12 h, 45.5%.

Scheme 2. Synthesis of the C_3-Symmetric Fullerene Tris-Adduct **6** and the All *e* [3:3]Hexakis-Adduct **7**[a]

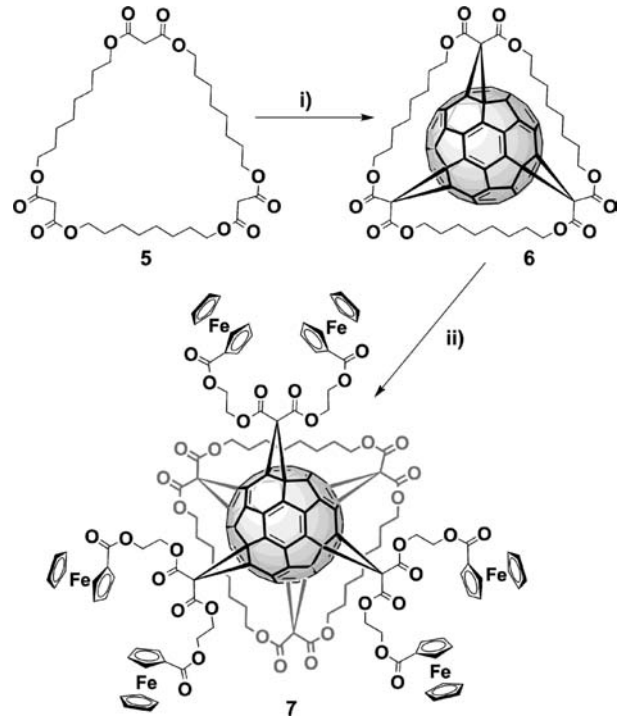

[a] (i) 1.0 equiv of C_{60}, 3.0 equiv of iodine, 6.0 equiv of DBU, toluene, room temperature, 6 h, 94%; (ii) (a) 5.0 equiv of DMA, toluene, room temperature, 4 h; (b) 3.0 equiv of **3**, 3.0 equiv of CBr_4, 6.0 equiv of DBU, room temperature, 24 h, 26.6%.

this purpose, ferrocene carboxylic acid **1** was coupled with ethylene glycol **2** as a short linker unit and subsequently reacted with malonyl dichloride.

The first example is the synthesis of the C_{2v}-symmetric monoadduct **4**. **4** is obtained in good yield after reacting malonate **3** with C_{60} in the presence of DBU and CBr_4 (Scheme 1). Complete structural characterization was performed by means of ^{1}H NMR, ^{13}C NMR, IR, and UV/vis spectroscopy as well as by mass spectrometry. For example, the number of resonances of C_{60} sp^2-C-atoms clearly proves the inherent C_{2v} symmetry. Because of two mirror planes, 5 and 12 signals with double and 4-fold intensity, respectively, are expected. In the region between 138 and 146 ppm, three signals with double intensity coalesce in the form of a single signal with, however, 4-fold intensity. The newly formed sp^3 centers of C_{60} resonate at 71.26 ppm.

To get access to C_{60} with six covalently attached ferrocene units, we used the tris-malonate **6** involving a C_3-symmetrical *e*,*e*,*e*-addition pattern as starting material, which is easily accessible via a highly regioselective tris-cyclopropanation of C_{60} with *cyclo*-[3]-octyl malonate **5** (Scheme 2).[22]

The subsequent completion of T_h-symmetrical addition pattern with three bis-ferrocenyl addends was accomplished by cyclopropanating the three remaining [6:6]-double bonds, at the equatorial positions, with **3** using a three-folding cyclopropanation mediated 9,10-dimethylanthracene (DMA) as a reversibly binding template (Scheme 2).[21] Use of a 5-fold excess of DMA results in an equilibrium between the various C_{60}DMA adducts, with *e*,*e*,*e*-$C_{60}DMA_3$ as the main component. Hence, synergetic combination of kinetic and thermodynamic control results in the generation of templates such as *e*,*e*,*e*-$C_{60}DMA_3$, with incomplete octahedral addition patterns. Because attack of irreversibly binding addends onto such templates occurs with highly pronounced regioselectivity at free octahedral sites and the reversibly bound DMA molecules can easily be replaced by the desired addends, hexakis-adducts with an octahedral addition pattern can be obtained in high yields. Because of the two different types of malonates, which per se give rise to an *e*,*e*,*e*-addition pattern each, the overall symmetry of **7** formed as a racemic mixture is C_3. The chiral nature of **7** is expressed in its ^{1}H NMR spectrum. The signals of the diastereotopic methylene protons of the glycol linker and the macrocyclic chain are seen in the region between 4.76 and 4.38 ppm and between 1.80 and 1.10 ppm. Two distinct regions in the spectrum corroborate the C_3-symmetry of **7**. In the sp^2-region of the fullerene core (148−140 ppm), 16 signals with 3-fold intensity are identified. These signals split into two sets (i.e., α and β). Such a splitting is characteristic for C_3-symmetrical hexakis-adducts that are made up by two different *e*,*e*,*e*-tris-adduct subunits.[23] In the region between 69.50 and 69.00 ppm, four signals with 3-fold intensity are observed as well. These signals are attributed to the 12 newly formed sp^3 C-atoms of the fullerene core.

The addition of six malonates led to the formation of the T_h-symmetrical hexakis-adduct **8** containing 12 covalently bound ferrocene units (Scheme 3). The high symmetry of **8** evokes a ^{1}H NMR spectrum that bears great resemblance to that of monoadduct **4**; only one set of signals that correlates with the H-atoms of the ferrocenes is registered. On the other hand, the ^{13}C NMR spectrum with two signals at 145.89 and 140.89 ppm confirms the T_h-symmetry. This is also reflected by the fact that all 12 newly formed sp^3 carbons of C_{60} give rise to only one signal at 68.94 ppm.

(23) Braun, M.; Hartnagel, U.; Ravanelli, E.; Schade, B.; Böttcher, C.; Vostrowsky, O.; Hirsch, A. *Eur. J. Org. Chem.* **2004**, 1983.

Scheme 3. Synthesis of the T_h-Symmetrical Fullerene Hexakis-Adduct **8**[a]

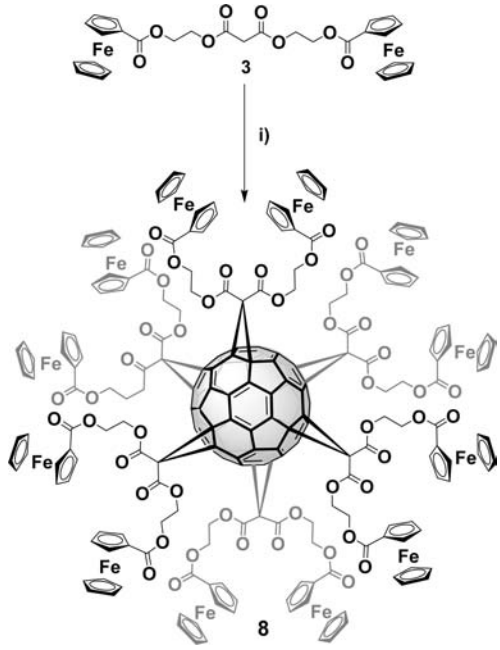

[a] (i) (a) 1.0 equiv of C_{60}, 10.0 equiv of DMA, toluene, room temperature, 4 h; (b) 6.0 equiv of CBr_4, 12.0 equiv of DBU, room temperature, 5 h, 12.3% (i.e., the reaction was carried out as a one-pot synthesis).

Similarly, [5:1]-hexakis-adducts **11**, **12**, **18**, and **19** bearing additional porphyrins were synthesized via a template-mediated approach using DMA (Scheme 4). For this purpose, the compounds **9**, **10**, **13**, and **14**, synthesized according to literature procedures procedures,[24,25] were chosen as starting materials. Using the malonates **9** and **15** as precursors, the monoadducts **10** and **16** were generated by nucleophilic cyclopropanation in the presence of iodine and DBU in toluene. After DMA activation, five ferrocenyl malonate building blocks **3** were connected to the remaining octahedral [6:6]-double bonds of **10** to afford the target [5:1]-hexakis-adduct **11**, which was subsequently converted into the zinc derivative **12** via metalation with $Zn(OAc)_2$. The ferrocene-free reference compounds **18** and **19** were synthesized similarly by cyclopropanation of the monoadduct **16** with malonate **17** and subsequent metalation with $Zn(OAc)_2$. An excess of both **3** and **17** was used to increase the yields of the corresponding hexakis-adducts **11** and **18**. The reaction was controlled by TLC and by analytical HPLC with UV/vis detection. All new mono- and hexakis-adducts **10**, **11**, **12**, **16**, **18**, and **19** were completely characterized by ^{1}H NMR, ^{13}C NMR, and UV/vis spectroscopy as well as by mass spectrometry.

Scheme 4. Synthesis of the [5:1]Hexakis-Adducts **11**, **12**, **18**, and **19**[a]

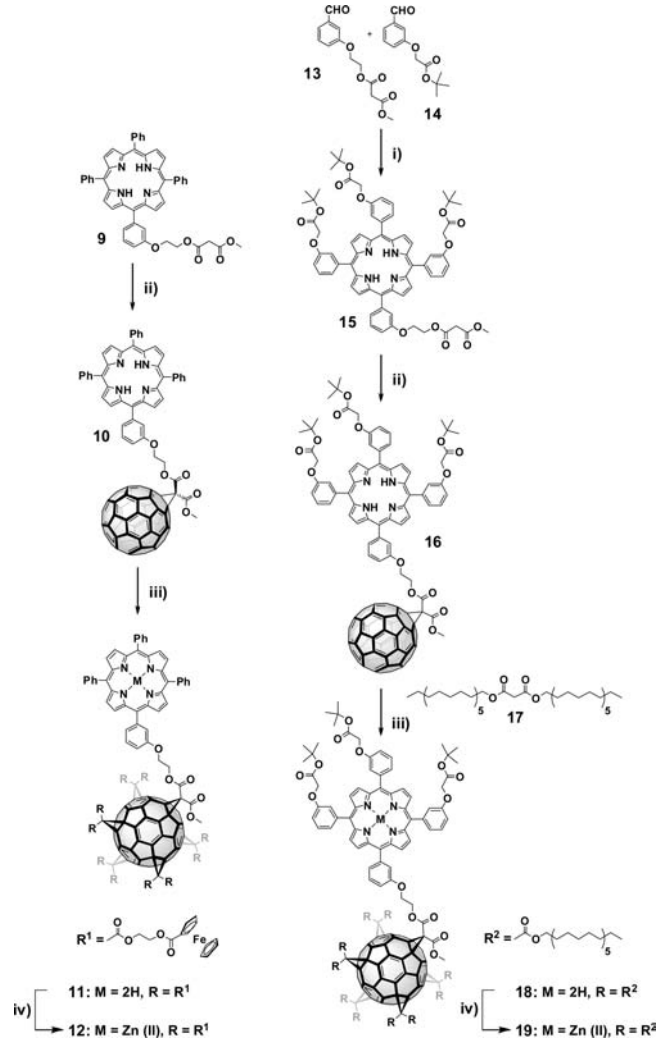

[a] (i) Pyrrole, $BF_3 \times Et_2O$, PPh_4Cl, EtOH, DDQ, CH_2Cl_2, yield: (**15**) 8%; (ii) iodine, DBU, toluene, C_{60}, 40−44%; (iii) DMA, DBU, CBr_4, toluene, **3** or **17**, 15−20%; (iv) $Zn(OAc)_2 \times 2H_2O$, THF, reflux, all 99%.

Free-base porphyrin **15** was synthesized according to a statistical condensation reaction under high-dilution conditions followed by oxidation with an excess DDQ as formerly described by Lindsey[25] and co-workers (Scheme 4). As expected for a statistical porphyrin reaction, lower and higher substituted derivatives (A4, A2B2 *trans*/*cis*, AB3, and B4) were obtained as well. Out of this mixture, **15** was isolated by column chromatography. The subsequent cyclopropanation of C_{60} with **15** afforded the monoadduct **16** in 44% yield. The conversion of the starting material was controlled via TLC, which was facilitated by quantitative fluorescence quenching, absent in **15**. The monoadduct **16** was collected as the second fraction during flash chromatography on silica gel using CH_2Cl_2 and $CHCl_3$ as eluents in a 1:2 ratio. As a general remark, we wish to emphasize that linking porphyrins like **15** to C_{60} necessitates the use of iodine instead of CBr_4. The latter is commonly employed when nonderivatized porphyrins are considered for modified BINGEL reactions. The [5:1]-hexakis-adducts **18** and **19** were synthesized to serve as reference compounds for the photophysical and electrochemical measurements.

As additional reference compounds for the following photophysical investigations, we also investigated porphyrin **20**[26]

(24) Guldi, D. M.; Hirsch, A.; Scheloske, M.; Dietel, E.; Troisi, A.; Zerbetto, F.; Prato, M. *Chem.–Eur. J.* **2003**, *9*, 4968.
(25) (a) Geier, G. R.; Lindsey, J. S. *J. Chem. Soc., Perkin Trans. 2* **2001**, 677. (b) Lindsey, J. S.; Schreiman, I. C.; Hsu, H. C.; Kearney, P. C.; Maguerettaz, A. M. *J. Org. Chem.* **1987**, *52*, 827. (c) Lindsey, J. S.; Wagner, R. W. *J. Org. Chem.* **1989**, *54*, 828. (d) Lindsey, J. S.; MacCrum, K. A.; Thyonas, J. S.; Chuang, Y.-Y. *J. Org. Chem.* **1994**, *59*, 579.
(26) Dietel, E.; Hirsch, A.; Zhou, J.; Rieker, A. *J. Chem. Soc., Perkin Trans. 2* **1998**, 1357.
(27) Brettreich, M.; Burghardt, S.; Böttcher, C.; Bayerl, T.; Bayerl, S.; Hirsch, A. *Angew. Chem.* **2000**, *112*, 1915; *Angew. Chem., Int. Ed.* **2000**, *39*, 1845.
(28) Kovacs, C.; Hirsch, A. *Eur. J. Org. Chem.* **2006**, 3348.
(29) Camps, X.; Dietel, E.; Hirsch, A.; Pyo, S.; Echegoyen, L.; Hackbarth, S.; Röder, B. *Chem.–Eur. J.* **1999**, *5*, 2362.

and fullerene derivatives **21**,[27] **22**,[28] and **23**,[23] which were synthesized according to protocols that we developed previously.

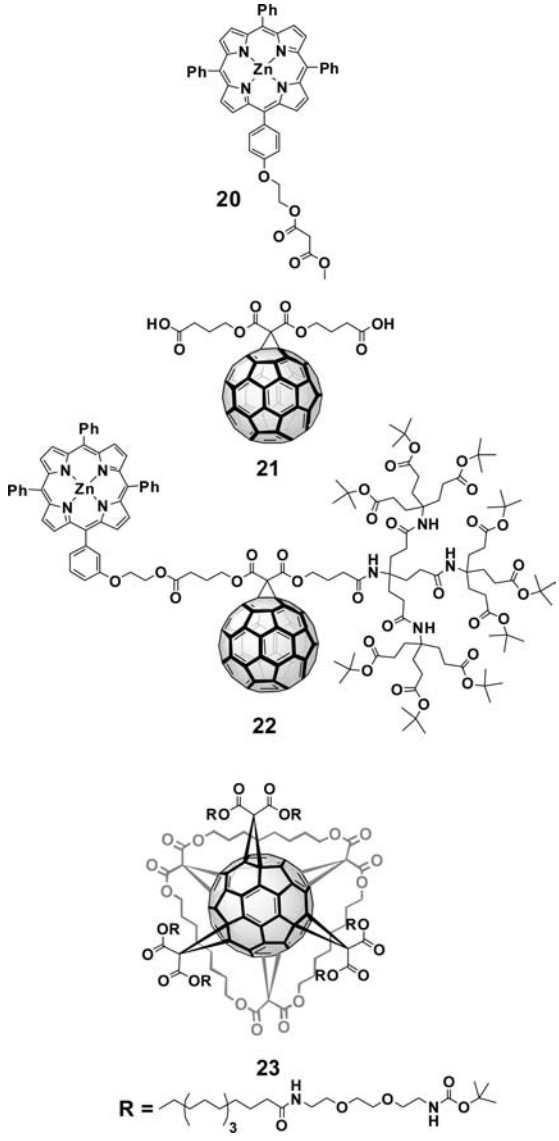

Absorption Spectroscopy. The electronic absorption spectra of the monoadducts (i.e., **21** and **4**) reflect the well-known absorption features with maxima at 209, 256, 328, 426, and 691 nm.[29] Still, upon closer inspection, a slight red-shift of approximately 2 nm has been derived from the differences between **4** and **21**. All of the hexakis-adducts (i.e., **23** and **8**) reveal drastically different electronic absorption spectra. The band at 256 nm splits, for instance, into two separate bands, one at 245 nm and another one at 269 nm with a shoulder at 283 nm. Further in the red, the band at 328 nm also splits, one at 318 nm and another one at 338 nm. The drastic changes observed in the electronic absorption spectra are a consequence of distorting the π-electronic structure of the fullerene.[29] Around 442 nm, the broad and weak absorptions of the ferrocene moieties occur for **8** with an extinction coefficient of about 100 M^{-1} cm^{-1} per ferrocene. When comparing **10** and **22** with the H_2P (**9**) and ZnP (**20**) references, the Soret- and Q-bands are red-shifted by 4 and 3 nm, respectively. In **18** and **19**, the absorption intensities of the Soret-bands are only 75% and 50% of what are seen for the H_2P and ZnP references, respectively.

Table 1. Electrochemical Data in MeCN with 0.1 M Bu_4NPF_6 as Supporting Electrolyte, at a Scan Rate of 100 mV s^{-1}[a]

	$MP^{\bullet+}/MP^{2+}$ [V]	$MP/MP^{\bullet+}$ [V]	$Fc/Fc^{\bullet+}$ [V]	$C_{60}/C_{60}^{\bullet-}$ [V]	$C_{60}^{\bullet-}/C_{60}^{2-}$ [V]	$MP/MP^{\bullet-}$ [V]
3			0.50			
4			0.55	−0.68	−1.21	
7			0.53	−1.30		
8			0.54	−1.31		
9		0.95				
10	1.25	0.95		−0.64		
11		0.97	0.65	−1.17	−1.60	
12		0.82	0.65	−1.12	−1.64	−1.47
18		0.95		−1.13		
19		0.77		−1.13		
20	1.00	0.77				−1.25
21				−0.65	−1.18	
22	1.05	0.77		−0.64		
23				−1.13		

[a] The potentials were measured versus a quasi Ag/Ag^+ reference electrode and converted versus SCE (i.e., +0.29 V).

The ground-state features of C_{60}, on the other hand, develop in the 200−400 nm range with maxima at 256, 327, and 370 nm. In contrast, the absorption spectra of **11** and **12** are just the superimpositions of the individual components.

Electrochemistry. The cyclic voltammogram of **4** discloses the first reduction of the fullerene at −0.68 V and oxidation of the two ferrocene units at +0.55 V in a 1:2 ratio (Table 1). Both processes are completely reversible and comparable with the values of the corresponding reference systems. From the energy gap, that is, the difference between the fullerene reduction and the ferrocene oxidation, we determine the radical ion pair state energy in THF as 1.23 eV.

When looking at **8**, the ferrocene oxidation potential remains virtually unchanged at +0.54 V. This indicates that there is no appreciable communication between the ferrocene moieties. On the other hand, the first reduction of the fullerene is shifted to −1.31 V. Each functional group that is added to C_{60} is known to shift the reduction to more negative potentials and to increase the irreversibility of the underlying process. In fact, in **8**, the conjugated part of the fullerene is that of a strained "cubic" cyclophane.[29,30] Correspondingly, the LUMO should be energetically raised, which renders it more difficult to accept electrons during, for example, the electrochemical and photochemical reduction experiments.

For **10**, only the reduction of the fullerene was clearly observable in the cyclic voltammogram at −0.64 V. The quasi-reversible oxidation of H_2P, on the other hand, at 0.95 V was only confirmed through differential pulse voltammetric experiments. The aforementioned **8** and **10** are particular helpful when interpreting the differential pulse voltammograms of **11**. Accordingly, the half wave potentials at +0.97 and at +0.55 V are assigned to the oxidation of H_2P and ferrocene, respectively. The relative intensities of the H_2P and ferrocene oxidation further support this assignment. Reduction occurs at −1.17 and at −1.60 V involving C_{60} and H_2P. Again, only the ferrocene oxidation gives rise to reversible processes in the cyclic voltammogram. Notably, the cathodic shift in **11** is not as pronounced as seen for **8**.

(30) (a) Boudon, C.; Gisselbrecht, J.-P.; Gross, M.; Isaacs, L.; Anderson, H. L.; Faust, R.; Diederich, F. *Helv. Chim. Acta* **1995**, *78*, 1334. (b) Cardullo, F.; Seiler, P.; Isaacs, L.; Nierengarten, J.-F.; Haldimann, R. F.; Diederich, F.; Mordasini-Denti, T.; Thiel, W.; Boudon, C.; Gisselbrecht, J.-P.; Gross, M. *Helv. Chim. Acta* **1997**, *80*, 343. (c) Diekers, M.; Hirsch, A.; Luo, C.; Guldi, D. M.; Bauer, K.; Nickel, U. *Org. Lett.* **2000**, *2*, 2741. (d) Bourgeois, J.-P.; Woods, C. R.; Cardullo, F.; Habicher, T.; Nierengarten, J.-F.; Gehrig, R.; Diederich, F. *Helv. Chim. Acta* **2001**, *84*, 1207.

The oxidation and reduction of ZnP in the reference and in **22** are identical, with potentials at +0.77 and −1.25 V, respectively. In general, the redox processes in **22** seem to be just the linear sum of those associated with the ZnP and the fullerene components.

In **12**, the reduction and oxidation potentials of some of the individual components are nearly overlapping. For example, on the reductive side, the C_{60} and ZnP centered processes are difficult to dissect. Only upon comparison with the reference systems is it possible to attribute the less anodic oxidation potential, at +0.65 V, to a ferrocene centered process, while the more anodic oxidation potential, at +0.82 V, correlates with that of the ZnP oxidation. The ratio of the cathodic currents also supports this assignment. Still more difficult is the interpretation of the reductive steps. The reduction potential at −1.12 V agrees well with the C_{60} reduction seen for the hexakis-adduct,[29−31] despite the 50 mV shift relative to **11**. This leaves the more anodic process at −1.47 V to correspond with the ZnP reduction.

Driving Force. The ion pair distances and ionic radii were estimated using semiempirical AM*1 geometry optimized models. The expression developed by Weller[32] helps to estimate the energies of the solvated ion pairs on the basis of the Born dielectric continuum model of the solvent:

$$-\Delta G_{CR} = e(E_{1/2}(D^{\bullet+}/D) - E_{1/2}(A^{\bullet-}/A)) + \Delta G_S \qquad (1)$$

$E_{1/2}(D^{\bullet+}/D)$ and $E_{1/2}(A^{\bullet-}/A)$ are the redox potentials of the donor and acceptor, respectively, and ΔG_S is the solvent correction factor, calculated by eq 2:

$$-\Delta G_S = \frac{e^2}{4\pi\varepsilon_0}\left[\left(\frac{1}{2R_+} + \frac{1}{2R_-} - \frac{1}{R_{D-A}}\right)\frac{1}{\varepsilon_S} - \left(\frac{1}{2R_+} + \frac{1}{2R_-}\right)\frac{1}{\varepsilon_R}\right] \qquad (2)$$

Here, ε_R is the dielectric constant of the solvent used for the determination of the redox potentials; ε_S is the dielectric constant of the solvent, in which the electron transfer occurs; R_+, R_- are the ionic radii of donor and acceptor, respectively; and R_{D-A} is the donor−acceptor distance. For the R_+, R_-, and R_{D-A} values, we relied on those that stem from the calculations. Finally, the free energy for charge separation ΔG_{CS} was determined using eq 3:

$$-\Delta G_{CS} = E_{0-0} - (-\Delta G_{CR}) \qquad (3)$$

The lowest lying excited-state energies (E_{0-0}) were estimated using absorption and fluorescence spectroscopy.

As a general feature, the energy of the radical ion pair states is significantly lower in polar solvents than in nonpolar solvents. In the monoadduct **4**, for example, the charge separation is barely possible in toluene, but when switching to more polar environments, the driving force for charge separation increases markedly (Table 2). When contrasting this to the hexakis-adduct **8**, the driving force for charge separation is decreased by a more cathodic fullerene reduction. The immediate consequence is that charge separation even in polar solvents, including THF, benzonitrile, and DMF, renders thermodynamically impossible.

Table 2. Driving Forces for Charge Separation and Charge Recombination Calculated in Accordance with the Dielectric Continuum Model[a]

	solvent	$-\Delta G_{CS}$ [eV]	$-\Delta G_{CR}$[b] [eV]	$-\Delta G_{CR}$[c] [eV]
4	PhMe	0.04	1.70	0.20
	THF	0.56	1.23	
	PhCN	0.92	0.87	
	DMF	0.95	0.84	
7	PhMe		2.30	0.80
	THF	0.02	1.83	0.33
	PhCN	0.38	1.47	
	DMF	0.41	1.44	
8	PhMe		2.33	0.82
	THF		1.85	0.35
	PhCN	0.36	1.49	
	DMF	0.39	1.46	
10	PhMe		2.02	0.62
	THF	0.30	1.59	0.19
	PhCN	0.59	1.30	
	DMF	0.62	1.27	
11	PhMe		2.51	1.11
	THF		2.14	0.74
	PhCN	0.05	1.84	0.44
	DMF	0.07	1.82	0.42
12	PhMe		2.33	0.83
	THF	0.10	1.94	0.44
	PhCN	0.39	1.65	0.15
	DMF	0.42	1.62	0.12
18	PhMe		2.50	1.10
	THF		2.04	0.64
	PhCN	0.14	1.75	0.35
	DMF	0.17	1.72	0.32
19	PhMe		2.31	0.81
	THF	0.14	1.90	0.40
	PhCN	0.43	1.61	0.11
	DMF	0.46	1.58	0.08
22	PhMe	0.19	1.85	0.35
	THF	0.63	1.41	
	PhCN	0.92	1.12	
	DMF	0.95	1.10	

[a] Dielectric constant, ε (for toluene, 2.4; THF, 7.6; benzonitrile, 24.9; DMF, 36.7). [b] Charge recombination to the ground state. [c] Charge separation to the lowest triplet excited state.

Fluorescence Spectroscopy. The excited-state features of **21** include a fluorescence maximum at 700 nm and a fluorescence quantum yield of 6.0×10^{-4}. The energy of the lowest vibrational state is estimated from the fluorescence spectra as 1.79 eV.[33] Moreover, this state decays rapidly within 1.8 ns to recover the singlet ground state. For **4**, on the other hand, we noted that the emission is completely quenched.

When going to the T_h-hexakis-adduct, the fluorescence features change dramatically, which partially evolves from the higher degree of fullerene functionalization.[33] For **22**, for example, the fluorescence quantum yield is with 2.3×10^{-3} ca. 4 times higher than the fluorescence quantum yield of **21**. The lowest singlet excited state is shifted from 1.79 eV (i.e., monoadduct) to 1.85 eV (i.e., T_h-hexakis-adduct). Nevertheless, the lifetime of this radiative deactivation was, as in the monoadduct and pristine C_{60}, determined to be 1.75 ns.

The fluorescence in **8** is quenched by more than a factor of 150, relative to **23**, leading to fluorescence quantum yields $<1.5 \times 10^{-6}$ and correspondingly to fluorescence lifetimes as short as 11 ps. Please note that such lifetimes are well beyond the instrumental resolution of our equipment of ~100 ps.

Figure 1 surveys the fluorescence spectra of **9**, **10**, **18**, and **11** with matching absorption at the excitation wavelength of

(31) Iehl, J.; de Freitas, R. P.; Delavaux-Nicot, B.; Nierengarten, J.-F. *Chem. Commun.* **2008**, 2450.
(32) Weller, A. *Z. Phys. Chem.* **1982**, *133*, 93.
(33) Guldi, D. M.; Hauke, F.; Hirsch, A. *Res. Chem. Intermed.* **2002**, *28*, 817.

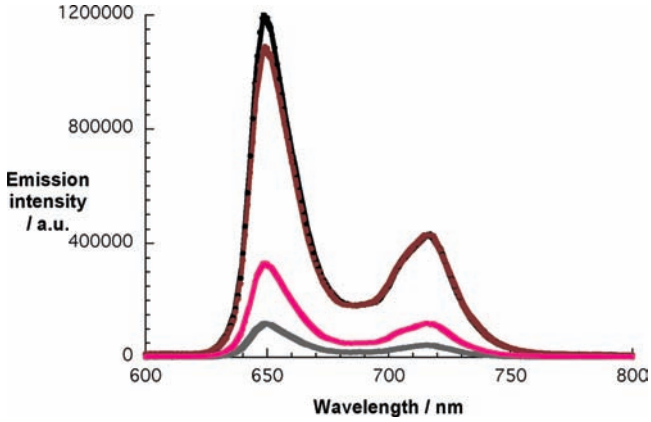

Figure 1. Steady-state fluorescence spectra of **9** (black spectrum), **10** (gray spectrum), **18** (brown spectrum), and **11** (red spectrum) in THF with matching absorption at the 416 nm excitation wavelength ($OD_{416nm} = 0.20$).

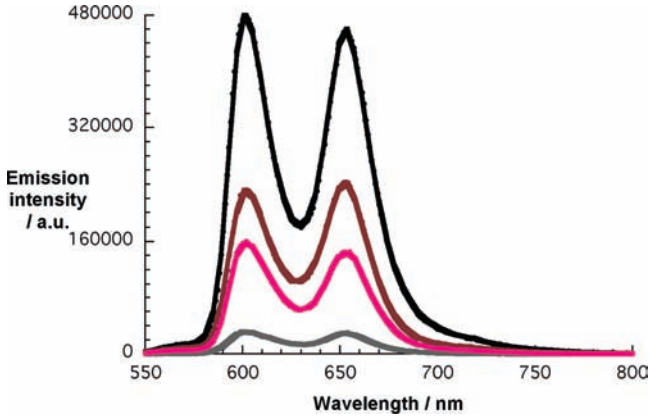

Figure 2. Steady-state fluorescence spectra of **20** (black spectrum), **22** (gray spectrum), **19** (brown spectrum), and **12** (red spectrum) in THF with matching absorption at the 410 nm excitation wavelength ($OD_{410nm} = 0.25$).

416 nm. **9** gives rise to the well-known emission at 650 and 716 nm with a fluorescence quantum yield and a fluorescence lifetime of 0.11 and 9.8 ns, respectively. The H_2P fluorescence is in **10** quenched nearly 10-fold, leading to a quantum yield of 0.011. No shifts of the emission bands were observed, and the fluorescence lifetime was determined to be 1.2 ns, which is in good agreement with comparable H_2P/C_{60} systems.[34] In stark contrast, the H_2P fluorescence is moderately quenched in **11**, with a quantum yield of 0.03 and a lifetime of 3.6 ns, and not affected at all for **18**, with a quantum yield of 0.10 and a lifetime of 9.8 ns.

The fluorescence behavior of the ZnP containing systems is similar to the aforementioned trends in the analogous H_2P systems; see Figure 2. **20** was found to exhibit the strongest fluorescence at 600 and 660 nm, from which a fluorescence quantum yield of 0.04 and a lifetime of 2.4 ns, both in excellent

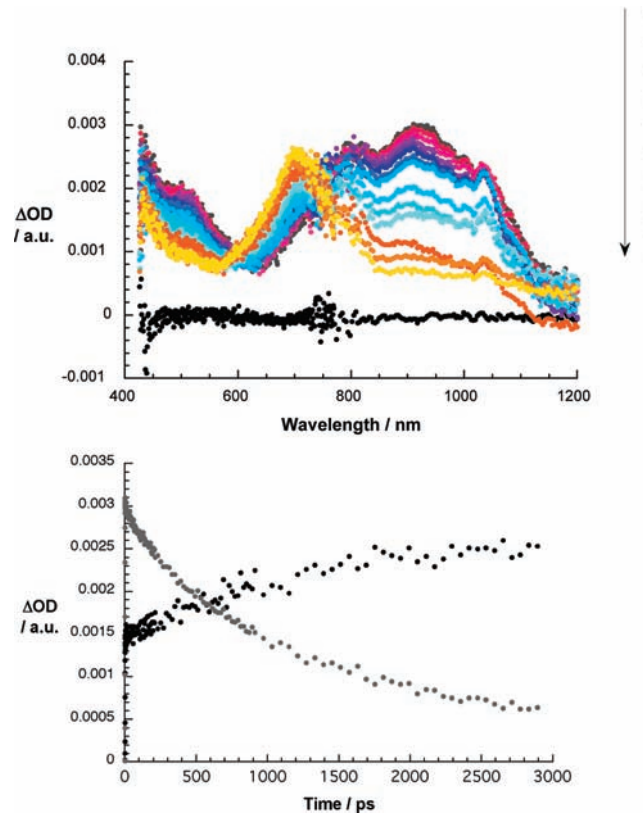

Figure 3. Top: Differential absorption spectra (visible and near-infrared) obtained upon femtosecond flash photolysis (387 nm) of **21** (2×10^{-4} M) in argon-saturated THF with several time delays between 0 and 3000 ps at room temperature; see legend for details about time progression. Bottom: Time−absorption profiles of the spectra shown above at 700 (black line) and 910 nm (gray line), monitoring the singlet to triplet intersystem crossing.

agreement with values found in the literature,[24,35] have been derived. The fluorescence spectrum of **22** yields a fluorescence quantum yield of 2.6×10^{-3}, from which we estimated a fluorescence lifetime of 169 ps. Weaker, on the other hand, are the interactions in the case of **12** and **19**, where the radiative pathway is only quenched 3 and 2 times, respectively. The fact that a change in solvent polarity, from, for example, toluene to benzonitrile, has literally no effect on the fluorescence quantum yields in the electron donor−acceptor conjugates prompts to a "through space" rather than "through bond" charge transfer deactivation.

Femto- and Nanosecond Laser Flash Photolysis. To characterize the transient intermediates involved in the deactivation of the fullerene and/or porphyrin excited states, a number of fast spectroscopic techniques were employed. In particular, transient absorption measurements were performed following either femto- or nanosecond laser excitation (i.e., 355, 388, 410, or 420 nm) in solvents of different polarity (i.e., toluene, THF, benzonitrile, or DMF). Pump wavelengths of 355 and 388 nm were used to photoactivate C_{60}, while either 410 or 420 nm was chosen to guarantee the excitation of ZnP or H_2P in their Soret region.

The photophysics of a reference compound of monosubstituted C_{60} **21** are shown in Figure 3 and are summarized as follows: The singlet excited state gives rise to a marked

(34) (a) Kuciauskas, D.; Lin, S.; Seely, G. R.; Moore, A. L.; Moore, T. A.; Gust, D.; Drovetskaya, T.; Reed, C. A.; Boyd, P. D. W. *J. Phys. Chem.* **1996**, *100*, 15926. (b) Vail, S. A.; Schuster, D. I.; Guldi, D. M.; Isosomppi, M.; Tkachenko, N.; Lemmetyinen, H.; Palkar, A.; Echegoyen, L.; Chen, X.; Zhang, J. Z. H. *J. Phys. Chem. B* **2006**, *110*, 14155. (c) Ohkubo, K.; Imahori, H.; Shao, J.; Ou, Z.; Kadish, K. M.; Chen, Y.; Zheng, G.; Pandey, R. K.; Fujitsuka, M.; Ito, O.; Fukuzumi, S. *J. Phys. Chem. A* **2002**, *106*, 10991.

(35) Luo, C.; Guldi, D. M.; Imahori, H.; Tamaki, K.; Sakata, Y. *J. Am. Chem. Soc.* **2000**, *122*, 6535.

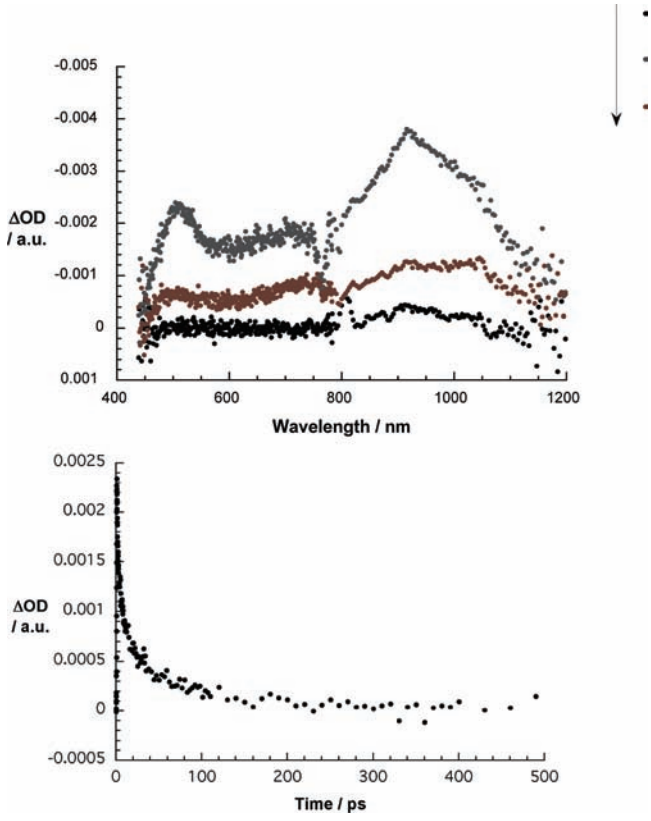

Figure 4. Top: Differential absorption spectra (visible and near-infrared) obtained upon femtosecond flash photolysis (387 nm) of **4** (2×10^{-4} M) in argon-saturated THF with time delays of 0 ps (black spectrum), 4 ps (gray spectrum), and 50 ps (brown spectrum) at room temperature; see legend for details about time progression. Bottom: Time−absorption profile of the spectra shown above at 500 nm, monitoring the charge separation and charge recombination.

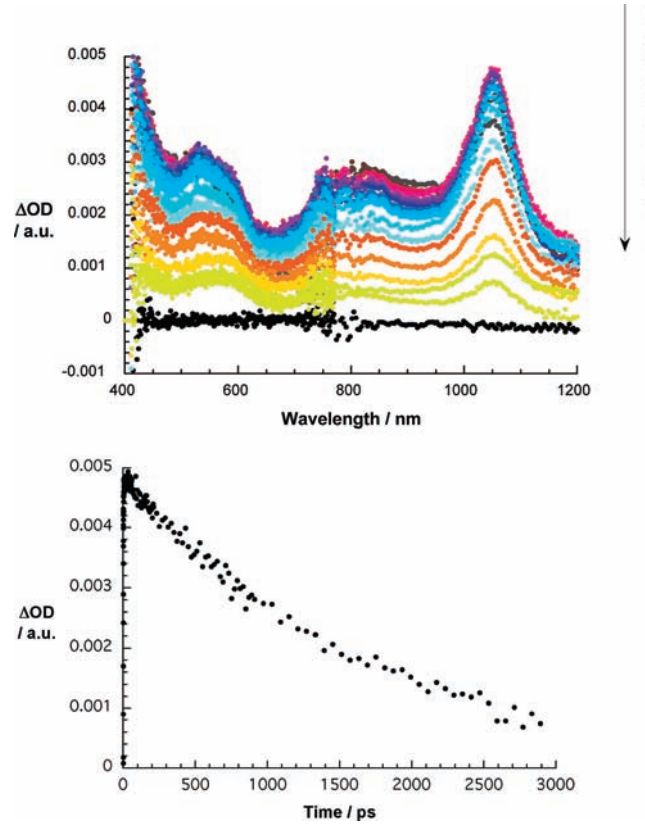

Figure 5. Top: Differential absorption spectra (visible and near-infrared) obtained upon femtosecond flash photolysis (387 nm) of **23** (2×10^{-4} M) in argon-saturated THF with several time delays between 0 and 3000 ps at room temperature; see legend for details about time progression. Bottom: Time−absorption profile of the spectra shown above at 1050 nm, monitoring the singlet to triplet intersystem crossing.

singlet−singlet absorption around 920 nm, whose lowest vibronic state has an energy of 1.79 eV.[34] Once generated, this state is subject to a rapid and quantitative intersystem crossing process to yield the energetically lower-lying triplet excited state (1.50 eV).[36] The intersystem crossing is quantitative and takes place with a rate constant of 7.4×10^8 s^{-1}, governed by large spin−orbit coupling.[34,36] The triplet−triplet absorption reveals a maximum in the visible region (720 nm), accompanied by another transition in the ultraviolet region (360 nm).

The excited-state properties of the C_{2v}-symmetric monoadduct with two ferrocene units **4** display, similar to **21**, the formation of the singlet excited state, which includes maxima in the visible and near-infrared region at 500 and 800−1000 nm, respectively. When comparing the absorption time profiles for **4** (Figure 4) with those of the C_{60} reference **21** (Figure 3), a different behavior is concluded. For **4**, the first singlet excited state decays within 10 ps to the 0.53 eV lower lying charge-separated radical ion pair state (1.23 eV), which subsequently recombines within 91 ps to the singlet ground state. Spectral characteristics of the radical ion pair state are the C_{60} radical anion at 1035 nm.[37] Considering that the charge separation outperforms the intersystem crossing (1.23 eV versus 1.50 eV), formation of the C_{60} triplet excited state evolves only as a minor pathway. This is also reflected in the transient absorption spectra, which lack appreciable triplet absorption. Charge separation and charge recombination were observed in all solvents. As expected, the dynamics are slower in toluene ($\tau_{CS} = 14$ ps; $\tau_{CR} = 127$ ps) than in the more polar solvents benzonitrile ($\tau_{CS} = 8$ ps; $\tau_{CR} = 78$ ps) or DMF ($\tau_{CS} = 4$ ps; $\tau_{CR} = 45$ ps). Neither spectral nor kinetic evidence would support any contribution from intersystem crossing in any of the cases.

A comparison of the T_h-hexakis-adduct (i.e., **23**) (Figure 5) with that of the monoadduct (i.e., **21**) (Figure 3) brings a number of drastic changes in the electronic structure of the fullerene to light. In particular, the singlet−singlet transitions are shifted to the red (i.e., 510 to 550 nm and 910 to 1050 nm), while the characteristic transient for the triplet excited state is barely visible at 590 nm. The singlet lifetime was determined as 1.66 ns, which is nearly identical to that reported for comparable systems (1.75 ns).[24,33,35] The triplet quantum yield of 0.15 for T_h-symmetrical hexakis-adducts, more than 6 times lower than that usually found in monofunctionalized C_{60}, helps to rationalize the weak transient absorptions. As discussed for **21**, the solvent polarity does not take any effect either on the lifetime of the singlet excited state or on the quantum yields of the singlet and triplet excited states.

Figure 6 exemplifies that for **8** a reactivity pattern is derived that bears partial resemblance to that of **23** and **4**. The fullerene

(36) (a) Guldi, D. M.; Asmus, K.-D. *J. Phys. Chem. A* **1997**, *101*, 1472. (b) Foote, C. S. *Top. Curr. Chem.* **1994**, *169*, 347.
(37) Guldi, D. M.; Prato, M. *Acc. Chem. Res.* **2000**, *33*, 695.
(38) The transient absorption band at 900 nm is assigned due to the fullerene radical anion, because the same absorption band was observed for the radical anion of T_h-$C_{66}(COOEt)_{12}$ in the pulse radiolytic reduction in oxygen-free 2-propanol, in which the solvated electron is the reducing entity.

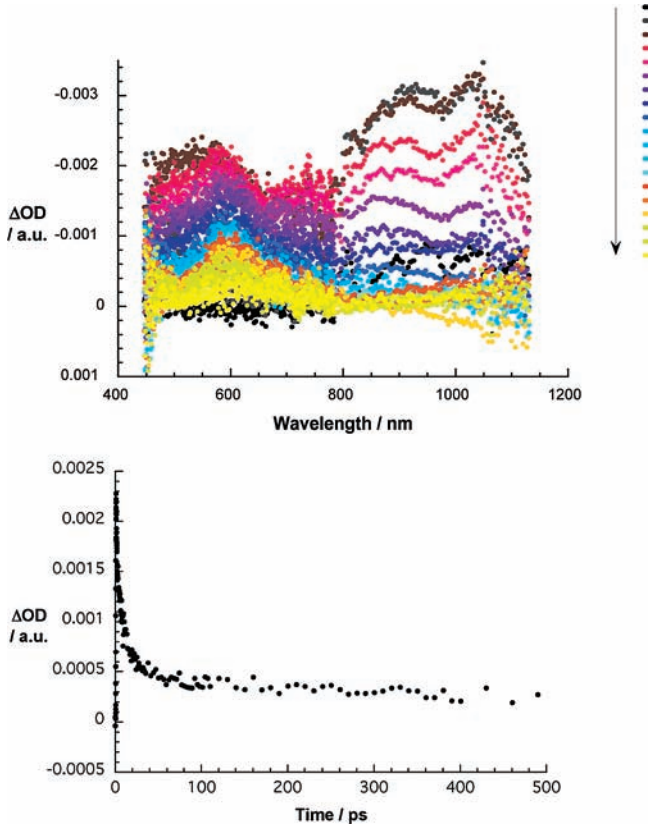

Figure 6. Top: Differential absorption spectra (visible and near-infrared) obtained upon femtosecond flash photolysis (387 nm) of **8** (2×10^{-4} M) in argon-saturated THF with several time delays between 0 and 3000 ps at room temperature; see legend for details about time progression. Bottom: Time−absorption profile of the spectra shown above at 600 nm, monitoring the accelerated intersystem crossing.

singlet excited state, which is formed instantaneously at 1050 nm, decays together with the radical anion that is observed at 900 nm.[38] By following the spectroscopic characteristics, even within the first few picoseconds a shift from 520 to 590 nm is discernible before disappearing entirely after about 59 ps. Such an intrinsic fast decay, together with the pronounced fluorescence quenching and the appearance of radical pair features, implies that the presence of 12 ferrocene units enhances the electron transfer from ferrocene to the fullerene singlet excited state to afford the radical ion pair that decays rapidly to the fullerene triplet excited state and that the triplet excited state (i.e., 590 nm) decays to the singlet ground state. Complementary performed transient absorption measurements in the nanosecond time regime confirmed the absence of any notable features. In summary, for **8** we determined singlet and triplet excited-state lifetimes of about 50 ps and between 3 and 13 ns (limited by the instrumental setups), respectively.

Table 3 summarizes the singlet excited lifetimes of the C_{60} references and the corresponding C_{60}/ferrocene donor−acceptor systems in a variety of solvents. The table documents solvent-independent intersystem crossing dynamics for the C_{60} references (i.e., **21** and **23**), while a strong solvent dependence is seen for the charge separation and the charge recombination steps in **4**.

The excited-state features of **9** differ strongly from the transients that were discussed in the context of the C_{60} systems. The visible region is, for example, dominated by intensive H_2P centered transitions, with ground-state absorption bleaching of

Table 3. Singlet Excited-State Energies, Fluorescence Data, Excited State, Charge Separation, and Charge Recombination Lifetimes, Determined via Femtosecond-Transient Absorption Measurements, for **1**, **4**, **8**, **9**, **10**, **11**, **12**, **18**, **19**, **20**, **21**, **22**, and **23** in Different Solvents[a]

	*S [eV]	solvent	Φ_F	τ_F [ps]	τ_{ISC} [ps]	τ_{CS} [ps]	τ_{CR} [ps]
1	2.46						
4	1.85	PhMe				14	127
		THF	1.5×10^{-6}	11[c]		10	91
		PhCN				8	78
		DMF				4	45
8	1.85	DMF	1.5×10^{-6}	11[c]	37[b]		
9	1.89	THF	0.11	9800	~10 000[b]		
		DMF	0.11	9800	~10 000[b]		
10	1.89	THF	0.011	1200		84	820
		PhCN				62	450
		DMF	9.5×10^{-3}	926		45	347
11	1.89	THF	0.03	3800			
		PhCN				46	
		DMF	1.8×10^{-2}	5000		43	496
12	2.04	THF	0.013	1200			
		PhCN				154	1256
		DMF	8.2×10^{-3}	1500		53	753
18	1.89	THF	0.10	8700			
		PhCN				900	
		DMF	6.0×10^{-2}	8100		53	424
19	2.04	THF	0.02	1500			
		PhCN				215	1366
		DMF	1.3×10^{-2}	1300		122	1005
20	2.04	THF	0.04	2400	2400[b]		
		DMF	0.04	2400	2400[b]		
21	1.79	THF	6.0×10^{-4}	1800	1350[b]		
		DMF	6.0×10^{-4}	1800	1350[b]		
22	2.04	PhMe				156	942
		THF	2.6×10^{-3}	189[c]		93	580
		PhCN				61	435
		DMF	1.5×10^{-3}	93[c]		17	228
23	1.79	THF	2.3×10^{-4}	1800	1660[b]		

[a] Transient absorption measurements were performed in all of the mentioned solvents, PhMe, THF, PhCN, and DMF. For the donor−acceptor conjugates, only the values for the electron transfer are mentioned. [b] Determined in all investigated solvents; see footnote a. [c] Estimated from the fluorescence quenching.

the Q-bands at 516, 549, 590, and 648 nm and maxima at 450, 532, 567, 620, and 674 nm followed by a broad and weak transient around 1050 nm in the NIR region. Initially (~2 ps), relaxation takes place from the higher excited states down to generate the first singlet excited state of **9**. Commencing with this internal conversion, an intersystem crossing starts to set in, which governs the photophysics of **9** over the course of approximately 10 ns.

The excited-state features of **10**, Figure 7, are dominated in the visible region by H_2P centered transitions, while the excited-state properties of C_{60} are observed in the near-infrared region. After a delay of 10 ps, the signature of the C_{60} radical anion ($C_{60}^{\bullet-}$) is discernible, revealing a characteristic band at 1035 nm.[37] Simultaneous with this formation, we record the growth of a broad transient in the visible (i.e., between 650 and 700 nm), which we ascribe to the H_2P radical cation. With this information in hand, we derived the charge separation (i.e., 84 ps) and charge recombination (i.e., 820 ps) kinetics in THF. By increasing the solvent polarity, the driving forces for charge separation and charge recombination increase and decrease, respectively. This is reflected in the following lifetimes: benzonitrile (62 and 450 ps) and DMF (45 and 347 ps). In toluene, on the other hand, only evidence for energy transfer and intersystem crossing emerged. Such a behavior reflects an energetic disposition of the radical ion pair state above that of the singlet excited precursors. Consequently, a negative driving

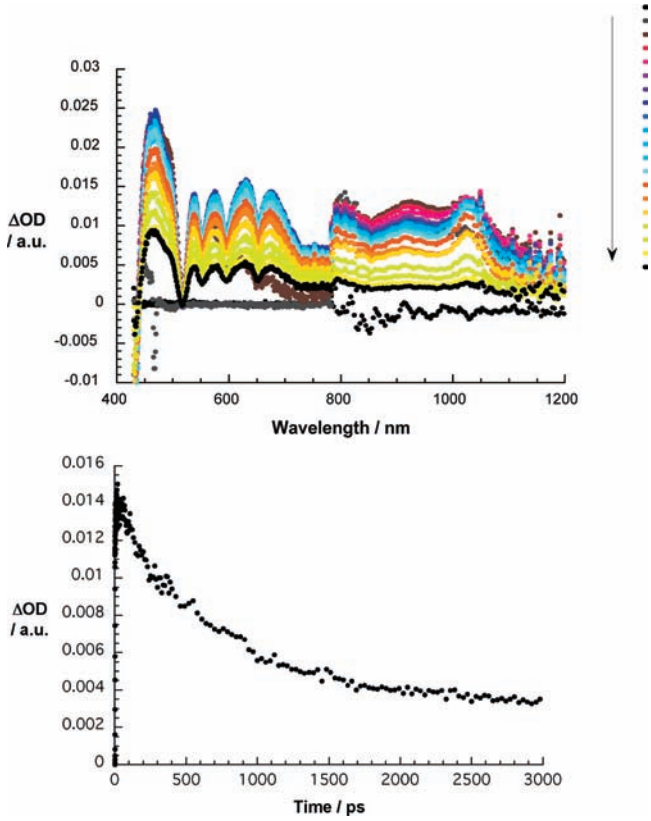

Figure 7. Top: Differential absorption spectra (visible and near-infrared) obtained upon femtosecond flash photolysis (410 nm) of **10** (1×10^{-5} M) in argon-saturated THF with several time delays between 0 and 3000 ps at room temperature; see legend for details about time progression. Bottom: Time−absorption profile of the spectra shown above at 1010 nm, monitoring the charge separation and charge recombination.

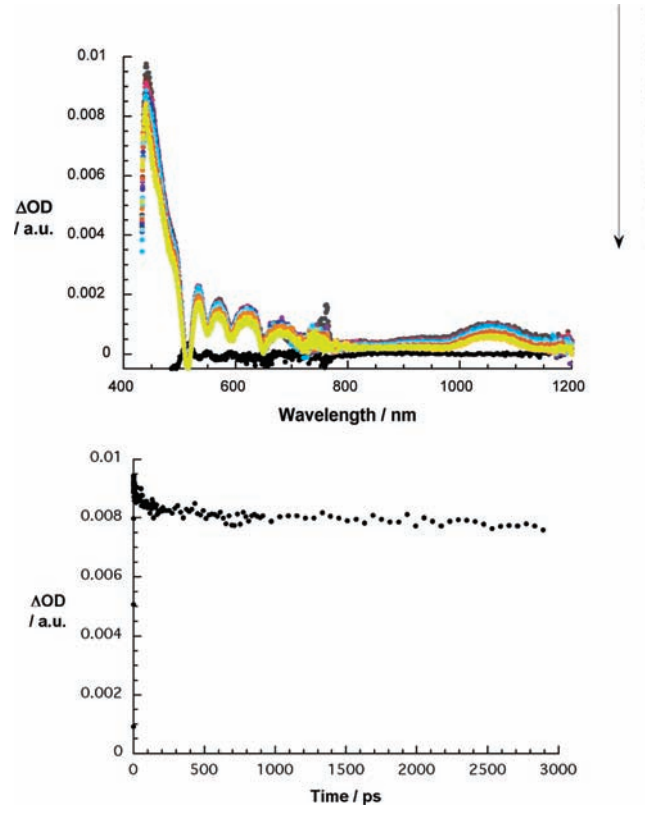

Figure 8. Top: Differential absorption spectra (visible and near-infrared) obtained upon femtosecond flash photolysis (410 nm) of **18** (1×10^{-5} M) in argon-saturated THF with several time delays between 0 and 3000 ps at room temperature; see legend for details about time progression. Bottom: Time−absorption profile of the spectra shown above at 445 nm, monitoring the singlet to triplet intersystem crossing.

force would evolve for the charge separation processes: −0.23 and −0.13 eV starting with the singlet excited states of H_2P and C_{60}, respectively.

When replacing the electron accepting monoadduct with the hexakis-adduct, significant changes are seen that are associated with the excited-state deactivation; see Figure 8. Important is that after 1 ps the singlet excited-state features of H_2P are registered, which subsequently decay via intersystem crossing. Relative to the aforementioned monoadduct, the charge separation channel is shut down, because the C_{60} reduction is shifted by about 0.5 eV. As a direct result, the energy of the radical ion pair state (2.08 eV) is placed above that of the H_2P singlet excited state (1.89 eV). In fact, a good correlation between transient absorption measurements and fluorescence experiments corroborates the postulate that, indeed, in toluene and THF no charge transfer occurs. Please also note that energy transfer is not feasible because of the nearly isoenergetic nature of the excited states. In more polar DMF, on the other hand, charge separation occurs within 53 ps. Hereby, the signatures of the H_2P radical cation and C_{60} radical anion develop before undergoing charge recombination within 424 ps.

When turning to **11**, Figure 9, it should be noted that the singlet excited states of H_2P and of C_{60} are isoenergetic (1.89 eV). This rules out the transduction of singlet excited-state energy between these two moieties. In fact, it leaves the following deactivation pathways: first, intersystem crossing to the corresponding triplet excited state of either H_2P or C_{60}; and, second, the direct decay to the ground state via fluorescence or via nonradiative processes. The charge separation is, however, a minor process, because of an insignificantly small energy gap in THF, 0.07 eV. The C_{60} singlet excited state lives for 1.30 ns, while H_2P intersystem crosses within 1.45 ns. Essentially similar are the observations for toluene and benzonitrile. Only in DMF does charge separation occur with 43 ps to yield a short-lived radical ion pair state, 496 ps.

The following transient absorption changes for the ZnP singlet excited state of a ZnP reference without C_{60} **20** are formed within 1 ps: a minimum, due to Q-band bleaching, at 550 nm and maxima at 500, 570−740, and 900−1000 nm. Within 2.4 ns, the singlet excited state (2.04 eV) transforms to the 0.51 eV lower-lying triplet excited state (1.53 eV)[24,35] via an efficient intersystem crossing in all measured solvents. For the latter, a triplet quantum yield of 0.88 emerged.

Next, the transient absorption changes of **22** were recorded. Figure 10 documents that at early times (1 ps) the transients are practically identical to those of the ZnP reference, besides the addition of the singlet excited-state features of C_{60} around 950 nm. After a short delay time of 3 ps, a new broad transition with maxima at 635 and 680 nm starts to grow in accompanied by another absorption at 1048 nm. On the basis of a spectral comparison, we ascribe the new bands in the visible region to the ZnP radical cation, while the band in the near-infrared belongs to the C_{60} radical anion.[36,37] The charge separation takes place with a time constant of 93 ps. Moreover, within 580 ps in THF, the subsequent charge recombination occurs. The ZnP triplet excited state must originate in part from the charge

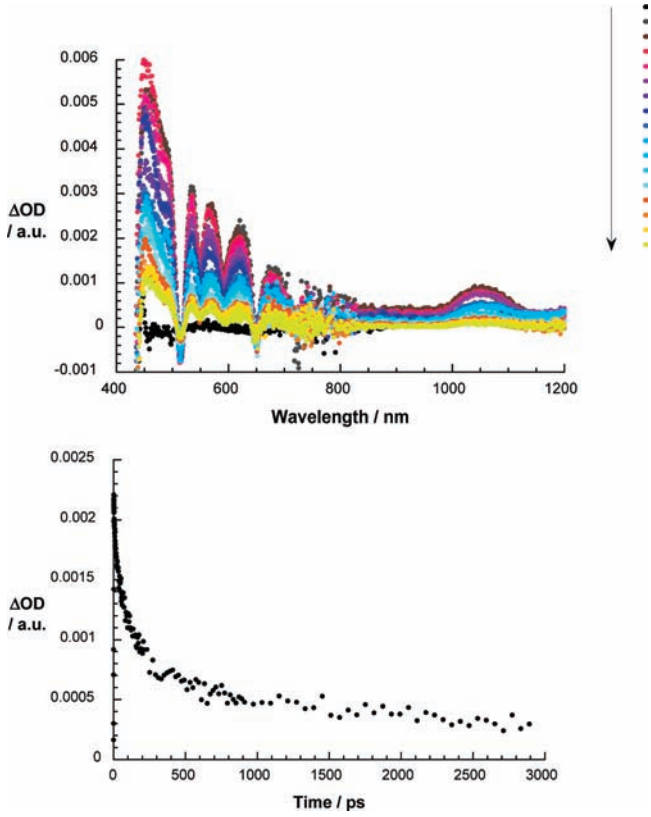

Figure 9. Top: Differential absorption spectra (visible and near-infrared) obtained upon femtosecond flash photolysis (410 nm) of **11** (1×10^{-5} M) in argon-saturated DMF with several time delays between 0 and 3000 ps at room temperature; see legend for details about time progression. Bottom: Time−absorption profile of the spectra shown above at 600 nm, monitoring the charge separation and charge recombination.

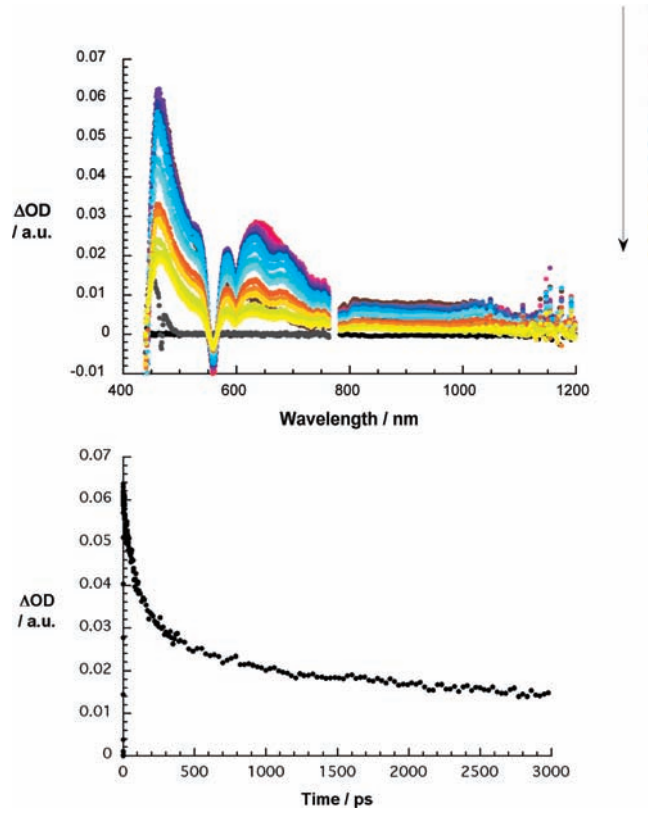

Figure 10. Top: Differential absorption spectra (visible and near-infrared) obtained upon femtosecond flash photolysis (410 nm) of **22** (1×10^{-5} M) in argon-saturated THF with several time delays between 0 and 3000 ps at room temperature; see legend for details about time progression. Bottom: Time−absorption profile of the spectra shown above at 460 nm, monitoring the charge separation and charge recombination.

recombination and in part from the singlet−singlet energy transfer, but is with an overall quantum yield of 0.22 about 4 times weaker than in the ZnP reference. Important is that we derive in benzonitrile and DMF shorter lifetimes of the radical ion pair state: 435 ps, benzonitrile; 228 ps, DMF. In contrast, the lifetime increases in toluene with a value of 942 ps. The charge separation is also accelerated in benzonitrile (61 ps) and DMF (17 ps).

For **19**, directly after laser excitation, the ZnP singlet excited state is discernible in the visible and in the NIR region of the spectra, vide supra. However, within 1.1 ns, the intersystem crossing takes place to form the ZnP triplet excited state. This is gathered in Figure 11. In toluene, a similar reactivity is derived. When turning to more polar solvents, the driving force for the charge separation increased to the point that formation of a radical ion pair state is enabled, 215 and 122 ps in benzonitrile and DMF, respectively. The recombination to the ground state, which is approximately 1.6 eV lower, is slow with values of 1366 ps in benzonitrile and 1005 ps in DMF. Such lifetimes constitute a significant improvement relative to **22**.

The last case deals with the excited-state properties of **12**. Directly after laser excitation, Figure 12, the singlet excited-state properties of ZnP and C_{60} are discernible (vide supra). Dominating is the ZnP singlet excited-state decay, which similar to that in **19** transforms within 1.2 ns to the ZnP triplet excited state. Competing with this pathway is an energy transfer to the 0.15 eV lower located C_{60} singlet excited state. Neither spectroscopic nor kinetic evidence was found in THF that would imply charge separation, to form the 0.1 eV lower-lying radical ion pair state (i.e., $ZnP^{+\bullet}-C_{60}^{\bullet-}-(Fc)_{10}$). Like in **19**, charge separation was, nevertheless, observed in the more polar media (i.e., benzonitrile and DMF). The characteristic ZnP radical cation bands are registered at 635 and 718 nm, while the maximum at 900 nm correlates well with the C_{60} radical anion absorption.[38] $ZnP^{+\bullet}-C_{60}^{\bullet-}-(Fc)_{10}$ may deactivate through a number of different pathways: first, the recombination to the ground state; second, the recombination to the lowest triplet excited state, being as in other C_{60} adducts around 1.50 eV;[33] and, third, charge shift from the ZnP radical cation to the 0.24 eV lower-lying Fc to yield subsequently $ZnP-C_{60}^{\bullet-}-(Fc)_{10}^{\bullet+}$ (1.38 eV). Our measurements provide, however, only support for the second pathway.

Energetics. In conclusion, **21** deactivates predominantly through intersystem crossing and weak fluorescence with a singlet excited-state lifetime of about 1.3 ns. The singlet excited state of **23**, although displaying a similar rate constant for the intersystem crossing, fluoresces much stronger and shifts to higher energies.

For the Fc-containing systems, **4** and **8**, new pathways for the C_{60} singlet excited-state deactivation evolve. The Fc centered singlet excited states (2.46 eV)[39] are not involved notably, either because of the low extinction coefficient of Fc at the excitation

(39) Sohn, Y. S.; Hendrickson, D. N.; Gray, H. B. *J. Am. Chem. Soc.* **1971**, *93*, 3603.

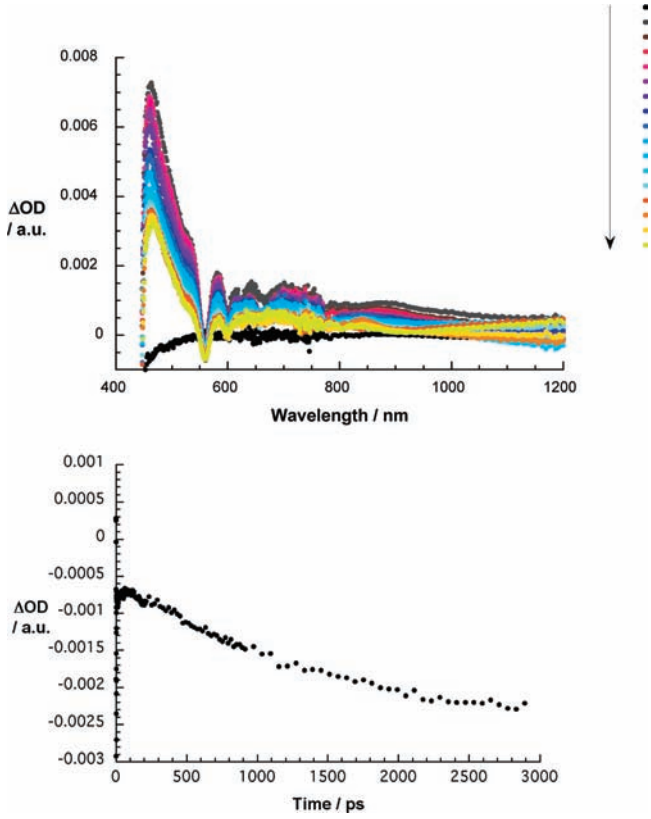

Figure 11. Top: Differential absorption spectra (visible and near-infrared) obtained upon femtosecond flash photolysis (410 nm) of **19** (1×10^{-5} M) in argon-saturated DMF with several time delays between 0 and 3000 ps at room temperature; see legend for details about time progression. Bottom: Time−absorption profile of the spectra shown above at 550 nm, monitoring the charge separation and charge recombination.

wavelength of 355 and/or 388 nm or due to a thermodynamically forbidden energy transfer pathway from the C_{60} singlet excited states (i.e., **21**, 1.79 eV; **23**, 1.85 eV). In **4**, the major deactivation pathway is that of charge separation, with a meaningful driving force of 0.56 eV. Charge recombination, which occurs in the Marcus inverted region, yields directly, without any triplet excited-state formation, the singlet ground state. In **8** (Scheme 5), not only the singlet excited-state energies are raised by about 0.06 eV, but also those of the radical ion pair states, which become close to being iso-energetic with the singlet excited states. Consequently, the charge separation channel is blocked. This leads us to consider only radiative and nonradiative pathways, bearing in mind that intersystem crossing finds a strong acceleration in these systems due to the presence of the multiple iron centers.

For **10**, the H_2P singlet excited state, located at 1.89 eV, is formed, which then decays via four different pathways. One of them is charge separation to yield the corresponding radical ion pair state (1.59 eV), which may evolve from either the H_2P (1.89 eV) or the C_{60} (1.79 eV) singlet excited state. The correspondingly formed radical ion pair recombines competitively to the lower lying H_2P triplet excited state (1.4 eV)[24,35] or to the ground state. Evidence for a possible C_{60} triplet excited-state formation (1.5 eV)[37] was not observed during our measurements.

(40) (a) Isaacs, L.; Wehrsing, A.; Diederich, F. *Helv. Chim. Acta* **1993**, *76*, 1231. (b) Scrivens, W. A.; Cassell, A. M.; North, B. L.; Tour, J. M. *J. Am. Chem. Soc.* **1994**, *116*, 6939.

Scheme 5. Energy Diagram of **8** and **12**

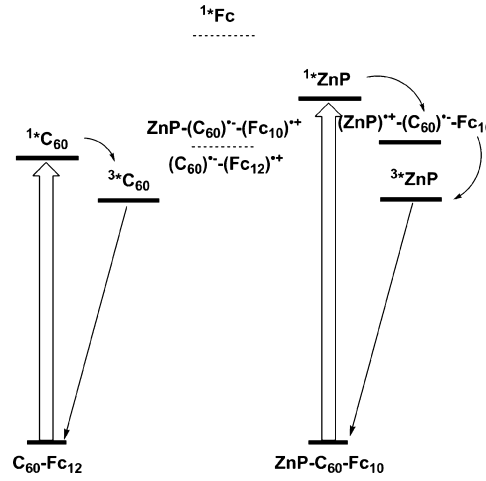

When comparing **22** (92.1%) with the aforementioned **10** (87.8%), higher quantum efficiencies (i.e., calculated via eq 4) for the charge separation are noticed.

$$\Phi_{CS} = \frac{\left[\left(\frac{1}{\tau_{diad}}\right) - \left(\frac{1}{\tau_{reference}}\right)\right]}{\left(\frac{1}{\tau_{diad}}\right)} \qquad (4)$$

This trends resembles the general finding with similar systems and is rationalized on the basis of different excited-state

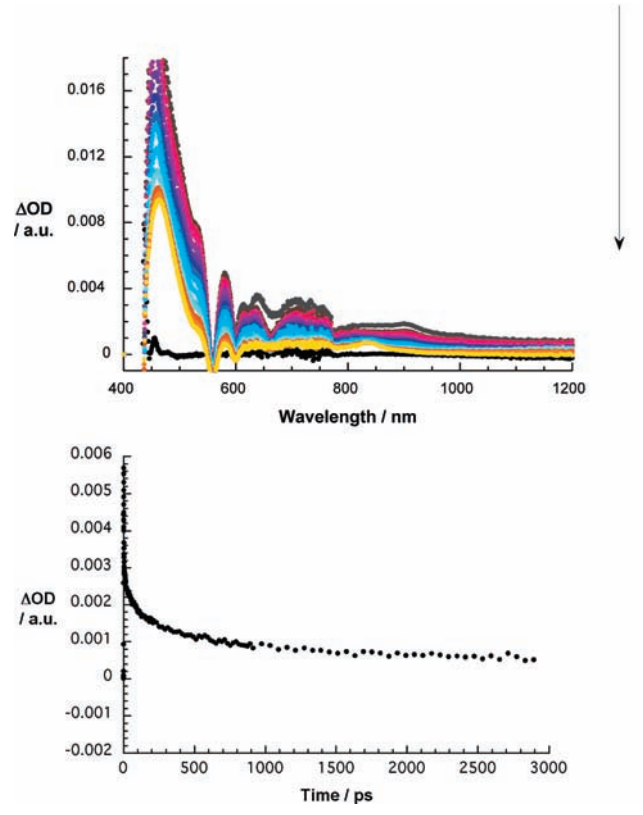

Figure 12. Top: Differential absorption spectra (visible and near-infrared) obtained upon femtosecond flash photolysis (410 nm) of **12** (1×10^{-5} M) in argon-saturated DMF with several time delays between 0 and 3000 ps at room temperature; see legend for details about time progression. Bottom: Time−absorption profile of the spectra shown above at 580 nm, monitoring the charge separation and charge recombination.

energies.[17] For example, the driving force for charge separation from the ZnP singlet excited state is 0.63 eV in THF. Such a driving force places the underlying charge transfer into the top region of the Marcus parabola. Even charge separation that would begin with the C_{60} singlet excited state is still fairly exothermic with 0.38 eV. The charge recombination takes an interesting twist. In polar media, the only exothermic pathway is the direct recovery of the singlet ground state. On the other hand, in nonpolar media, formation of the ZnP triplet excited state is thermodynamically within reach.

Next, the energetics that are associated with the hexakis-adducts, **18** and **19**, shall be discussed. The ZnP and H_2P singlet excited states are located at 2.04 and 1.89 eV, respectively. Please note that this implies no changes at all relative to what has been concluded for the corresponding **10** and **22**. In toluene and THF, two dominant pathways are energetically feasible: intersystem crossing and/or singlet energy transfer. In benzonitrile and DMF, besides the aforementioned processes, charge separation is able to compete. This may occur either from the ZnP or H_2P singlet excited state or from the C_{60} singlet excited state: The energies are 1.78 and 1.58 eV in DMF. The correspondingly formed radical ion pairs recombine competitively to either the ZnP or the H_2P triplet excited state (1.53 eV[24,35] and 1.40 eV[24,35]), the lower lying C_{60} triplet excited state (1.50 eV), or even the ground state.

We now take a closer look into the processes that may take place in **11** and **12**. As discussed already for the C_{60} references, the reduction of C_{60} renders more difficult upon the 6-fold functionalization. As a result, the energy of the radical ion pair state increases from 1.59 eV ($H_2P^{\bullet+}-C_{60}^{\bullet-}$) to 2.14 eV ($H_2P^{\bullet+}-C_{60}^{\bullet-}-(Fc)_{10}$) and is now located above the singlet excited state of H_2P (1.89 eV). Obviously, charge separation that would evolve from the H_2P singlet excited state renders impossible with the exception of the very polar media, a conclusion that has been corroborated by our femtosecond experiments. So, deactivation, following the initial photoexcitation into the Soret-band, is limited to energy transfer to the C_{60} singlet excited state (1.85 eV) or intersystem crossing. Charge separation from the C_{60} singlet excited state to form the fullerene radical anion and the ferrocene radical cation ($H_2P-C_{60}^{\bullet-}-(Fc)_{10}^{\bullet+}$) remains as a minor process. Replacing H_2P with ZnP in, for example, **12** (Scheme 5) raises the energy of the porphyrin singlet excited states above that of the radical ion pair state. This, in turn, opens the pathway for charge separation in some cases, vide supra. In THF, however, the decay of the ZnP singlet excited state (2.04 eV) hardly populates the 0.1 eV lower lying radical ion pair state ($ZnP^{\bullet+}-C_{60}^{\bullet-}-(Fc)_{10}$). Instead, the 0.19 eV lower lying C_{60} singlet excited state and/or the ZnP triplet excited state are populated. In more polar media, the energy of the radical ion pair state drops below that of the initially formed ZnP singlet excited state. As a direct consequence, charge separation does occur to produce the radical ion pair state ($ZnP^{\bullet+}-C_{60}^{\bullet-}-(Fc)_{10}$). This state recombines to the ZnP triplet excited state and the ground state. As an alternative, a charge shift reaction to afford the charge-shifted radical ion pair ($ZnP-C_{60}^{\bullet-}-(Fc)_{10}^{\bullet+}$) is energetically feasible. This radical ion pair would also decay to the lower-lying ZnP triplet excited state. Thus, incorporation of Fc units provides no apparent advantage with respect to charge transfer properties of these materials, as recognized by comparison of the properties of **18** and **19**, which do not have attached Fc moieties, with **11** and **12**, which have Fc moieties (vide supra). Incorporation of stronger electron donor units than Fc units may be required to attain the charge-shifted radical ion pair.

Conclusions

We have successfully synthesized and characterized a series of mono- and hexakis-adducts of C_{60} that contain up to 12 ferrocenes or 10 ferrocenes and one porphyrin. Notable is the fact that the electron acceptor ability of C_{60} is significantly impacted by the addition pattern, which enables fine-tuning of the energies of the radical ion pair states. Charge transfer from ferrocene to the C_{60} singlet excited state is only exothermic in the case of the monoadduct of C_{60}, while in the hexakis-adduct of C_{60} it renders endothermic. In stark contrast, incorporating ZnP into the hexakis-adducts of C_{60} (i.e., together with 10 ferrocene units) and the proper choice of solvent have allowed us to power an exothermic electron transfer that evolves from the ZnP singlet excited state to the hexakis-adducts of C_{60}. Although the radical ion pair state lifetimes are in the order of a nanosecond, hexakis-adducts of C_{60} provide a unique platform for the construction of multicomponent electron donor−acceptor ensembles. Nevertheless, the full utilization of hexakis-adducts of C_{60}, ensuring fast charge separation in combination with slow charge recombination, might be accomplished by implementing rigid linkers that connect the electron donors and electron acceptors. Rigid linkers assist in governing charge transfer interactions that are driven by a "through bond" mechanism. Such a strategy has been documented to function in suppressing rapid charge recombination, which in the present systems is facilitated by "through space" interaction of the electron donors and electron acceptors.

Experimental Section

Chemicals. C_{60} was obtained from Hoechst AG/Aventis and separated from higher fullerenes by a plug filtrationy.[40] All analytical-reagent grade solvents were purified by distillation. Dry solvents were prepared using literature procedures.

Thin Layer Chromatography (TLC). Riedel-de-Haen silica gel F_{254} and Merck silica gel 60 F_{254}. Detection: UV lamp and iodine chamber.

Preparative Thin Layer Chromatography (PTLC). Merck PLC plates 20 × 20 cm; silica gel 60 F_{254}, 2 mm.

Flash Chromatography (FC). Merck silica gel 60 (230−400 mesh, 0.04−0.063 nm).

High Performance Liquid Chromatography (HPLC), Analytical. Shimadzu liquid chromatograph LC-10 with Bus modul CBM-10A, auto injector SIL-1 OA, two pumps LC-10AT, diode array detector. The HPLC-grade solvents were purchased from SDS or Acros Organics; analytical column Nucleosil 5 μm, 200 × 4 mm, Macherey-Nagel, Düren.

High Performance Liquid Chromatography (HPLC), Preparative. Shimadzu Class LC 10 with Bus module CBM-10A, auto injector SIL-10A, two pumps LC-8A, UV detector SPD-10A, fraction collector FRC-10A. Solvents were purified by distillation prior to use.

IR Spectroscopy. Bruker FT-IR Vector 22, KBr pellets, ν values in cm^{-1}.

UV/Vis Spectroscopy. Shimadzu UV-3102 PC, UV−vis−NIR scanning spectrophotometer; absorption maxima λ_{max} are given in [nm].

Mass Spectroscopy. Micromass Zabspec, FAB(LSIMS) mode, matrix 3-nitrobenzylalcohol (NBA).

NMR Spectroscopy. JEOL JNM EX 400 and JEOL JNM GX 400 and Bruker Avance 300. The chemical shifts are given in ppm relative to TMS. The resonance multiplicities are indicated as *s*

(singlet), *d* (doublet), *t* (triplet), *q* (quartet), and *m* (multiplet), nonresolved and broad resonances as *br*.

Elementary Analysis. (C, H, N) succeeded by combustion and gas chromatographical analysis with an EA 1110 CHNS analyzer (CE Instruments).

Electrochemistry. Electrochemical experiments were carried out using a BAS-CV50W electrochemical workstation with positive feedback compensation. Cyclic voltammetry, differential pulse voltammetry, and square wave voltammetry were performed in a three-electrode cell with a platinum wire as counter electrode, a glassy carbon disk as working electrode (Ø = 2 mm) versus a nonaqueous Ag/Ag^+ reference electrode (0.01 M $AgNO_3$ in dry MeCN). Afterward, the values of the potentials were recalculated versus SCE. Tetra-*n*-butylammonium hexafluorophosphate (Bu_4NPF_6 − 0.1 M) was used as supporting electrolyte, and all experiments were performed under an argon atmosphere.

Steady-State Fluorescence Spectroscopy. Horiba Jobin Yvon Fluoromax 3 spectrophotometer; in deaerated solution at room temperature (298 K) in a 1 to 1 cm quartz cuvette. All spectra were corrected for the instrument response. The monitoring wavelength corresponded to the maximum of the emission band. For excitation wavelength below 450 nm, a cut off filter (450 nm) was inserted.

Time-Resolved Fluorescence. Fluorescence lifetimes were measured with a laser strope fluorescence lifetime spectrometer (Photon Technology International) with 337 nm laser pulses (800 ps) from a nitrogen laser fiber-coupled to a lens-based T-formal sample compartment equipped with a stroboscopic detector. Fluorescence lifetimes were measured at the emission maximum at room temperature in deaerated solution in a 1 to 1 cm quartz cuvette.

Femtosecond-Transient Absorption Spectroscopy. Femtosecond-transient absorption studies were performed with 387 nm laser pulses (1 kHz, 150 fs pulse width, 200 nJ) from an amplified Ti/sapphire laser system (model CPA 2101, Clark-MXR Inc. − output 775 nm). For an excitation wavelength of 420 nm, a nonlinear optical parametric converter (NOPA) was used to generate ultra short tunable visible pulses out of the pump pulses. The transient absorption pump probe spectrometer (TAPPS) is referred to as a two-beam setup, where the pump pulse is used as the excitation source for transient species, and the delay of the probe pulse is exactly controlled by an optical delay rail. As probe (white light continuum), a small fraction of pulses stemming from the CPA laser system was focused by a 50 mm lens into a 2 mm thick sapphire disk. The transient spectra were recorded using fresh oxygen-free solutions in each laser excitation. All experiments were performed at 298 K in a 2 mm quartz cuvette.

Nanosecond-Transient Absorption Spectroscopy. Transient absorption experiments, based on nanosecond laser photolysis, were performed with the output of the third harmonics (355 nm) coming from a Nd/YAG laser (Brilliant, Quantel). Moreover, pulse widths of <5 ns with an energy of 10 mJ were selected. The optical detection is based on a pulsed Xenon lamp (XBO 450, Osram), a monochromator (Spectra Pro 2300i, Acton Research), a R928 photomultiplier tube (Hamamatsu Photonics), or a fast InGaAs photodiode (Nano 5, Coherent) with 500-MHz amplification and a 1 GHz digital oscilloscope (WavePro7100, LeCroy). The laser power of every laser pulse was registered by using a bypath with a fast silicon photodiode. The nanosecond-laser photolysis experiments were performed by using 1 cm quartz cells, and the solutions were saturated with argon if no other gas saturation is indicated.

General Remarks. All fullerene derivatives discussed in this study have been synthesized and stored under an inert gas atmosphere (argon or nitrogen); no special requirements like glove boxes are needed for sample storage and handling. Sample characterization was performed in degassed solvents without further prerequisites.

2-Hydroxyethyl Ferrocenecarboxylate (2). In a dry 250 mL flask with addition funnel were dissolved 1 g (4.35 mmol) of ferrocene carboxylic acid, 3 mL of ethylene glycol, and 105 mg of DMAP (0.2 equiv) in 150 mL of dry CH_2Cl_2 under an argon atmosphere. The solution was cooled to 0 °C by an ice/water bath. A solution of 897 mg (1.0 equiv) of DCC in 50 mL of dry CH_2Cl_2 was added slowly over 1 h. The reaction mixture was allowed to warm to room temperature and stirred for 12 h. The reaction mixture was concentrated in vacuo, and the precipitated DCU was removed by suction filtration. Purification of **2** was carried out by flash chromatography (silica, CH_2Cl_2/EtOAc 8:2). Evaporation of the solvent yielded an orange solid. Yield: 92.2%. ^{1}H NMR ($CDCl_3$, 400 MHz): δ = 4.80 (*m*, 2H, −CH *cp*), 4.39 (*m*, 2H, −CH *cp*), 4.35 (*m*, 2H, $-CO_2-CH_2$), 4.19 (8, 5H, −CH *cp*), 3.88 (*m*, 2H, $-CO_2-OH$), 2.38 (t, ^3J = 5.6 Hz, 1H, −COOH) ppm. ^{13}C NMR ($CDCl_3$, 100.4 MHz): δ = 172.45 (1C), 71.49 (2C), 70.47 (1C), 70.16 (2C), 69.81 (5C), 65.95 (1C), 61.65 (1C) ppm. IR (KBr): ν = 3542, 3444, 3331, 3101, 3087, 3000, 2956, 2914, 2871, 2851, 1683, 1461, 1414, 1378, 1284, 1238, 1222, 1146, 1106, 1078, 1029, 1002, 925, 915, 890, 875, 846, 820, 794, 771, 615, 595, 538, 504, 483, 460, 412 cm^{-1}. UV/vis (CH_2Cl_2): λ_{max} (log ε) = 310 (3.03), 347 (2.56), 446 (2.37) nm. MS (EI): *m*/*z* = 274 $[M]^+$. Anal. Calcd for $C_{13}H_{14}FeO_3$ (274.09): C, 56.97; H, 5.15; Fe, 20.37; O, 17.51. Found: C, 56.78; H, 4.98.

Bis-{2-[(ferrocenylcarbonyl)oxy]ethyl}malonate (3). In a dry 250 mL flask were dissolved 1 g (3.65 mmol) of 2-hydroxyethyl ferrocenecarboxylate **2** and 295 μL (1.0 equiv) of pyridine in 100 mL of dry CO_2Cl_2 under an argon atmosphere. The solution was cooled to 0 °C by an ice/water bath. 177.5 μL (0.5 equiv) of malonyl dichloride was added to the solution. The reaction mixture was allowed to warm to room temperature and stirred for 2 h. Afterward, the reaction mixture was concentrated in vacuo. Purification of **3** was carried out by flash chromatography (silica, CH_2Cl_2/EtOAc 9:1). The solvent was removed in vacuo, and the product was subsequently redissolved in a minimum amount of CH_2Cl_2 and precipitated out of *n*-pentane. Yield: 68.8%. ^{1}H NMR ($CDCl_3$, 400 MHz): δ = 4.79 (*m*, 4H, −CH *cp*), 4.42 (*m*, 8H, $-CH_2CH_2-$), 4.38 (*m*, 4H, −CH *cp*), 4.18 (*s*, 10H, −CH *cp*), 3.48 (8, 2H, $CO-CH_2-CO$) ppm. ^{13}C NMR ($CDCl_3$, 100.4 MHz): δ = 171.44 (2C), 166.03 (2C), 71.49 (4C), 70.37 (2C), 70.19 (4C), 69.80 (10C), 63.48 (2C), 61.55 (2C), 41.18 (1C) ppm. IR (KBr): ν = 3108, 3094, 3085, 3012, 2962, 2853, 1749, 1738, 1709, 1461, 1412, 1397, 1376, 1344, 1326, 1267, 1201, 1142, 1117, 1050, 1032, 1019, 1008, 960, 920, 873, 848, 820, 775, 680, 609, 576, 543, 507, 483, 460, 417 cm^{-1}. UV/vis (CH_2Cl_2): λ_{max} (log ε) = 309 (3.35), 347 (2.88), 447 (2.68) nm. MS (EI): *m*/*z* = 616 $[M]^+$. Anal. Calcd for $C_{29}H_{28}Fe_2O_8$ (616.22): C, 56.52; H, 4.58; Fe, 18.13; O, 20.77. Found: C, 56.33; H, 5.02.

Bis-{2-[(ferrocenylcarbonyl)oxy]ethoxycarbonyl} Methano-1,2-[60]fullerene (4). In a dry 250 mL flask were dissolved 260 mg (375 μmol) of C_{60}, 231 mg (1.0 equiv) of bis-{2-[(ferrocenylcarbonyl)oxy]ethyl}malonate **3**, and 124 mg (1.0 equiv) of CBr_4 in 150 mL of dry toluene under argon. 66.2 μL (2.0 equiv) of DBU was added, and the reaction mixture was stirred for 12 h at room temperature. The reaction mixture was concentrated in vacuo. Purification of **4** was carried out by flash chromatography (silica, toluene/EtOAc 9:1). The solvent was removed in vacuo, and the product was redissolved in a minimum amount of CS_2 and precipitated out of *n*-pentane. Yield: 45.4%. ^{1}H NMR (CS_2/$CDCl_3$, 400 MHz): δ = 4.78 (m, 8H, −CH *cp* + $-CH_2-$), 4.58 (m, 4H, $-CH_2-$), 4.36 (m, 4H, −CH *cp*), 4.21 (s, 10H, −CH *cp*) ppm. ^{13}C NMR (CS_2/$CDCl_3$, 100.4 MHz): δ = 171.46 (2C), 163.27 (2C), 145.23 (4C), 145.15 (4C), 145.03 (4C), 144.92 (4C), 144.87 (2C), 144.64 (4C), 144.58 (4C), 144.55 (2C), 143.79 (4C), 143.05 (2C), 142.97 (4C), 142.91 (4C), 142.14 (4C), 141.84 (4C), 140.89 (4C), 138.99 (4C), 71.62 (4C), 71.26 (2C), 70.36 (4C), 70.25 (2C), 69.91 (10C), 65.20 (2C), 61.50 (2C), 51.74 (1C) ppm. IR (KBr): ν = 3108, 3094, 3085, 3013, 2986, 2952, 1750, 1716, 1708, 1460, 1438, 1411, 1395, 1375, 1351, 1277, 1230, 1206, 1186, 1139, 1108, 1052, 1024, 1011, 923, 814, 770, 738, 703, 577, 550, 526, 500, 482, 459 cm^{-1}. UV/vis (CH_2Cl_2): λ_{max} (log ε) = 258 (5.12), 326 (4.59), 394 (3.66), 426 (3.39), 483 (3.21) nm. MS (FAB, NBA): *m*/*z* = 1335

$[M]^+$, 720 $[C_{60}]^+$. Anal. Calcd for $C_{89}H_{26}Fe_2O_8$(1334.48) × $2CS_2$: C, 73.50; H, 1.76; Fe, 7.51; O, 8.61; S, 8.62. Found: C, 74.12; H, 1.99.

***e*,*e*,*e*,*e*,*e*,*e*-(*cyclo*-[3]-Octylmalonyl)-tris-[di-(2-[(ferrocenylcarbonyl)oxy]ethoxycarbonyl}methano]dodecahydro[60]fullerene (7).** In a dry 250 mL flask with addition funnel were dissolved 300 mg (221 μmol) of *e*,*e*,*e*-(*cyclo*-[3]-octylmalonyl)hexahydro[60]-fullerene **6** and 228 mg (5.0 equiv) of 9,10-dimethylanthracene in 100 mL of dry toluene under argon. The reaction mixture was stirred for 4 h at room temperature without exposure to light. 409 mg (3.0 equiv) of bis-{2-[(ferrocenylcarbonyl)oxy]ethyl}malonate **3** and 220 mg (3.0 equiv) of CBr_4 were added. A solution of 218 μL (6.0 equiv) of DBU in 25 mL of dry toluene was added dropwise. The reaction mixture was stirred for 24 h at room temperature. Purification of **7** was carried out by flash chromatography (silica, toluene/EtOAc 7:3) with subsequent HPLC separation (nucleosil, toluene/EtOAc 8:2). The solvent was removed in vacuo, and the product was redissolved in a minimum amount of CS_2 and precipitated out of *n*-pentane. Yield: 26.6%. ^{1}H NMR ($CDCl_3$, 400 MHz): δ = 4.76 (m, 12H, −CH *cp*), 4.61 (m, 6H, $-OCH_2-$), 4.49 (m, 12H, $-OCH_2-$), 4.38 (m, 24H, −CH *cp* + $-OCH_2-$), 4.16 (s, 30H, CH *cp*), 4.11 (m, 6H, $-OCH_2-$), 1.8−1.1 (m, 36H, $-CH_2-$) ppm. ^{13}C NMR ($CDCl_3$, 100.4 MHz): δ = 171.32 (6C), 163.45/163.16/163.01/162.95 (each 3C), 146.49 (3C), 145.86 (3C), 145.73 (3C), 145.70 (3C), 145.20 (3C), 145.14 (3C), 145.07 (3C), 144.79 (3C), 142.15 (3C), 141.91 (3C), 141.36 (3C), 141.25 (3C), 140.97 (3C), 140.88 (3C), 140.57 (3C), 140.40 (3C), 71.53 (12C), 70.20 (18C), 69.82 (60C), 69.24/69.17/69.04/69.01 (each 3C), 66.92/66.28 (each 3C), 64.68/64.59 (each 3C), 61.32 (6C), 46.67/44.99 (each 3C), 29.17/29.10/28.70/26.22/25.55 (18C) ppm. IR (KBr): ν = 3104, 3095, 2956, 2927, 2855, 1748, 1716, 1460, 1396, 1376, 1352, 1274, 1214, 1134, 1080, 1051, 1024, 923, 822, 760, 714, 669, 528, 501, 485, 458 cm^{-1}. UV/vis (CH_2Cl_2): λ_{max} (log ε) = 244 (5.09), 269 (4.97), 279 (4.94), 309 (4.72), 335 (4.61) nm. MS (FAB, NBA): *m*/*z* = 3200 $[M]^+$, 1600 $[M]^{2+}$, 720 $[C_{60}]^+$. Anal. Calcd for $C_{180}H_{126}Fe_6O_{36}$ (3200.34) × C_7H_8: C, 68.22; H, 4.10; Fe, 10.18; O, 17.50. Found: C, 67.56; H, 5.01.

1,2:18,36:22,23:27,45:31,32:55,56-Hexakis-{di-(2-[(ferrocenylcarbonyl)oxy]ethoxycarbonyl}methano}dodecahydro[60]fullerene (8). In a dry 250 mL flask with addition funnel were dissolved 200 mg (278 μmol) of C_{60} and 573 mg (10.0 equiv) of 9,10-dimethylanthracene in 125 mL of dry toluene under argon. The reaction mixture was stirred for 4 h at room temperature without exposure to light. One gram (6.0 equiv) of bis-{2-[(ferrocenylcarbonyl)oxy]ethyl}malonate **3** and 552 mg (6.0 equiv) of CBr_4 were added. A solution of 498 μL (12.0 equiv) of DBU in 25 mL of dry toluene was added dropwise. The reaction mixture was then stirred for 5 h at room temperature. Purification of **8** was carried out by flash chromatography (silica, toluene) with subsequent HPLC separation (nucleosil, toluene/EtOAc 8:2). The solvent was removed in vacuo, and the product was redissolved in a minimum amount of CS_2 and subsequently precipitated out of *n*-pentane. Yield: 12.3%. ^{1}H NMR ($CDCl_3$, 400 MHz): δ = 4.75 (m, 24H, −CH *cp*), 4.45 (m, 24H, $-OCH_2-$), 4.37 (m, 48H, −CH *cp* + $-OCH_2-$), 4.16 (s, 60H, −CH *cp*) ppm. ^{13}C NMR ($CDCl_3$, 100.4 MHz): δ = 171.26 (12C), 163.08 (12C), 145.89 (24C), 140.89 (24C), 71.53 (24C), 70.20 (36C), 69.83 (120C), 68.94 (12C), 64.71 (12C), 61.27 (12C), 44.78 (6C) ppm. IR (KBr): ν = 3104, 3095, 2956, 2927, 2868, 2854, 1749, 1714, 1460, 1396, 1376, 1350, 1276, 1212, 1136, 1107, 1080, 1045, 1025, 921, 822, 772, 715, 669, 530, 501, 485, 458 cm^{-1}. UV/vis (CH_2Cl_2): λ_{max} (log ε) = 243 (5.20), 268 (5.07), 310 (4.78), 335 (4.63), 438 (3.63) nm. MS (FAB, NBA): *m*/*z* = 4405 $[M + H]^+$, 3791 $[M]^+ - (\mathbf{3})$, 3177 $[M]^+ - [2\times(\mathbf{3})]$, 2559 $[M]^+ - [3\times(\mathbf{3})]$, 720 $[C_{60}]^+$. Anal. Calcd for $C_{234}H_{156}Fe_{12}O_{48}$ (4405.85) × $2C_7H_8$: C, 64.89; H, 3.78; Fe, 14.60; O, 16.73. Found: C, 62.51; H, 4.11.

11. In a dry 250 mL flask with addition funnel were added 250 mg (168 μmol) of **13** and 346 mg (1.68 μmol, 10.0 equiv) of 9,10-dimethylanthracene in 100 mL of dry toluene under nitrogen. The reaction mixture was stirred for 3 h at room temperature without exposure to light. 1.04 g (1.68 mmol, 10.0 equiv) of **3** and 557 mg (1.68 mmol, 10.0 equiv) of CBr_4 were subsequently added. A solution of 0.5 mL (3.36 mmol, 20.0 equiv) of DBU in 50 mL of dry toluene was added slowly and dropwise. The reaction mixture was stirred for 83 h at room temperature. Purification of **11** was carried out by flash chromatography (silica, toluene/EtOAc 8:2) with subsequent HPLC separation (nucleosil, CH_2Cl_2). The solvent was removed in vacuo, and the product was redissolved in a minimum amount of CH_2Cl_2 and precipitated out of *n*-pentane. Yield: 29.9%. ^{1}H NMR (400 MHz, $CDCl_3$): δ = −2.79 (br, 2H, −NH), 3.74 (s, 3H, $-OCH_3$), 4.20 (m, 50H, −CH *cp*), 4.41 (m, 20H, −CH *cp*), 4.48 (m, 44H, $-CH_2$), 4.77 (m, 20H, −CH *cp*), 7.29−7.77 (m, 11H, *p*-ArH, *m*-ArH), 8.11−8.29 (m, 8H, *o*-ArH), 8.85 (br, 8H, βH-pyr) ppm. ^{13}C NMR (100.4 MHz, $CDCl_3$): δ = 51.00 (6C, malonyl-C), 53.89 (1C, $-OCH_3$), 61.37 (10C, $-OCH_2CH_2$), 63.51 (1C, $-OCH_2CH_2$), 64.76 (10C, $-OCH_2CH_2$), 65.47 (1C, $-OCH_2CH_2$), 69.89 (80C, *cp* CH and *ipso-cp* C), 70.25 (20C, −CH *cp*), 71.58 (12C, C_{60} sp^3C), 114.08 (1C, *o*-ArC), 120.18 (4C, *meso*-C), 126.67, 127.72 (4C, *p*-ArC), 128.02, 128.15 (9C, *m*-ArC), 131.10 (8C, βC-pyr), 134.53 (8C, *o*-ArC), 140.96, 141.61 (4C, *ipso*-C), 143.63, 145.89, 145.99 (48C, $C_{60}-sp^2C$), 163.20 (1C, ArCO), 167.01 (2C, $-\underline{C}O_2CH_2CO_2$ and $-CO_2CH_2\underline{C}O_2$), 171.38 (10C, $-\underline{C}O_2CH_2CO_2$ and $-CO_2CH_2\underline{C}O_2$) ppm. IR (KBr): ν = 3313, 3030, 2934, 1734, 1623, 1505, 1474, 1431, 1428, 1311, 1266, 1213, 1179, 1177, 1081, 1035, 999, 961, 893, 879, 854, 778, 753, 691 cm^{-1}. UV/vis (CH_2Cl_2): λ_{max} = 261, 270, 312, 340, 400, 418, 480, 515, 549, 589, 645 nm. MS (FAB, NBA): *m*/*z* = 4565 $[M]^+$, 4264, 3965. Anal. Calcd for $C_{255}H_{166}Fe_{10}N_4O_{45}$(4564.50) × CH_2Cl_2 × EtOAc: C, 65.92; H, 3.74; Cl, 1.50; Fe, 11.79; N, 1.18; O, 15.87. Found: C, 65.68; H, 4.02; N, 1.09.

12. Compound **11** (40 mg, 8.76 μmol) and 5 mg (19.0 μmol) of zincacetate dihydrate in dried THF (50 mL) were stirred for 12 h under reflux in an argon atmosphere. The flash chromatographic purification of the metalated porphyrin was carried out with silica and dichloromethane/ethylacetate as eluents in a ratio of 1:1. Afterward, the polarity of the eluents was increased. After evaporation of the concentrated organic phases, the product was obtained as a red brown solid in quantitative yield. ^{1}H NMR (400 MHz, $CDCl_3$): δ = 3.78 (s, 3H, $-OCH_3$), 4.18 (m, 50H, −CH *cp*), 4.38 (m, 20H, −CH *cp*), 4.46 (m, 44H, $-CH_2$), 4.72 (m, 20H, −CH *cp*), 5.58 (t, ^3J = 4.0 Hz, $-OCH_2CH_2$), 5.67 (t, ^3J = 4.0 Hz, $-OCH_2CH_2$), 7.32−7.95 (m, 11H, *p*-ArH, *m*-ArH), 8.04−8.31 (m, 8H, *o*-ArH), 8.91 (br, 8H, βH-pyr) ppm. ^{13}C NMR (100.4 MHz, $CDCl_3$): δ = 51.09 (6C, malonyl-C), 53.79 (1C, $-OCH_3$), 61.34 (10C, $-OCH_2CH_2$), 63.48 (1C, $-OCH_2CH_2$), 64.72 (10C, $-OCH_2CH_2$), 65.49 (1C, $-OCH_2CH_2$), 69.86 (80C, *cp* CH and *ipso-cp* C), 70.25 (20C, −CH *cp*), 71.56 (12C, C_{60} $-sp^3$C), 120.93 (4C, *meso*C), 126.48, 127.40 (4C, *p*-ArC), 128.15 (9C, *m*-ArC), 131.89 (8C, βC-pyr), 134.45 (8C, *o*-ArC), 140.96, 142.90, 145.99 (52C, C_{60} $-sp^2$C and *ipso*-C), 163.17 (1C, ArCO), 171.19, 171.38 (10C, $-\underline{C}O_2CH_2CO_2$ and $-CO_2CH_2\underline{C}O_2$) ppm. IR (KBr): ν = 3024, 2950, 1736, 1596, 1575, 1470, 1441, 1349, 1176, 1150, 966, 800, 733, 699 cm^{-1}. UV/vis (CH_2Cl_2): λ_{max} = 263, 270, 313, 342, 421, 549, 588 nm. MS (FAB, NBA): *m*/*z* = 4628 $[M]^+$. Anal. Calcd for $C_{255}H_{164}Fe_{10}N_4O_{45}Zn$ (4627.89) × $2CH_2Cl_2$ × EtOAc: C, 64.16; H, 3.63; Cl, 2.90; Fe, 11.43; N, 1.15; O, 15.39; Zn, 1.34. Found: C, 62.72; H, 4.41; N, 1.55.

15. The synthesis of porphyrin **15** was performed under standard conditions with $BF_3 \times Et_2O$.[25] 2-(3-Formylphenoxy)ethyl-methylmalonate (2.66 g, 10 mmol), *t*-butyl-2-(3-formylphenoxy)acetate (2.36 g, 10 mmol), 1H-pyrrole (1.35 mL, 20 mmol), $BF_3 \times Et_2O$ (1.27 mL, 10 mmol), DDQ (3.40 g, 15 mmol), and NEt_3 (2.0 mL) were dissolved in 1.5 L of CH_2Cl_2 under argon. The flash chromatographic purification was carried out with silica and CH_2Cl_2 as eluent. The purple red solid was obtained in 13% yield. ^{1}H NMR (400 MHz, $CDCl_3$): δ = −2.84 (br, 2H, −NH), 1.45 (s, 27H, $-C(CH_3)_3$), 3.48 (s, 2H, $-CO_2CH_2CO_2$), 3.70 (s, 3H, $-OCH_3$),

4.39 (t, ^3J = 4.4 Hz, 2H, $-OCH_2CH_2$), 4.60 (t, ^3J = 4.3 Hz, 2H, $-OCH_2CH_2$), 4.71 (s, 6H, $-OCH_2CO_2{}^t$Bu), 7.35 (dd, ^2J = 7.8 Hz, 1H, *p*-ArH), 7.64−7.76 (m, 4H, *m*-ArH), 7.78−7.86 (m, 8H, *o*-ArH), 8.87 (br, 8H, βH-pyr) ppm. ^{13}C NMR (100.4 MHz, $CDCl_3$): δ = 28.02 (9C, $-C(CH_3)_3$), 41.18 (1C, $-CO_2CH_2CO_2$), 52.55 (1C, $-OCH_3$), 63.84 (1C, $-OCH_2CH_2$), 65.75 (1C, $-OCH_2CH_2$), 65.85 (3C, $-CH_2CO_2-{}^t$Bu), 82.43 (3C, $-C(CH_3)_3$), 114.19, 114.40 (4C, *p*-ArC), 119.63 (4C, *meso*-C), 120.83, 121.09 (4C, *o*-ArC), 127.62 (4C, *m*-ArC), 128.17, 128.37 (4C, *o*-ArC), ca. 130.90 (8C, βC-pyr), 143.38, 143.54 (4C, *ipso*-C), 156.28, 156.76 (11C, α-C and ArCO), 166.50 (1C, ArCO), 166.64, 166.76 (2C, $-\underline{C}O_2CH_2CO_2$, $-CO_2CH_2\underline{C}O_2$), 167.97 (1C, $-CO_2-{}^t$Bu) ppm. IR (KBr): ν = 3440, 3019, 2930, 1810, 1602, 1570, 1469, 1439, 1351, 1289, 1173, 1068, 1042, 999, 968, 938, 870, 844, 798, 776, 749, 726, 694, 633 cm^{-1}. UV/vis (CH_2Cl_2): λ_{max} = 400, 418, 513, 549, 589, 643 nm. MS (FAB, NBA): *m*/*z* = 1165 $[M]^+$, 1109, 997. Anal. Calcd for $C_{68}H_{68}N_4O_{14}$ (1664.47) × 2EtOAc: C, 68.04; H, 6.31; N, 4.18; O, 21.47. Found: C, 67.84; H, 4.53; N, 4.35.

16. In a dry 1.0 L flask with addition funnel were dissolved 597 mg (0.83 mmol) of C_{60}, 757 mg (0.64 mmol) **15**, and 196 mg (0.77 mmol, 1.2 equiv) iodine in 400 mL of dry toluene under argon. 140 μL (0.94 mmol, 1.5 equiv) of DBU, dissolved in additional 150 mL of dry toluene, was added slowly and dropwise. The reaction mixture was then stirred for 12 h at room temperature. The reaction mixture was concentrated in vacuo. Purification of **16** was carried out by flash chromatography (silica, toluene/EtOAc 9:1). The solvent was removed in vacuo, and the product was redissolved in a minimum amount of CH_2Cl_2 and precipitated out of *n*-pentane. Yield: 41.7%. ^{1}H NMR (400 MHz, $CDCl_3$): δ = −2.99 (br, 2H, −NH), 1.44 (s, 18H, $-C(CH_3)_3$), 1.55 (s, 9H, $-C(CH_3)_3$), 3.98 (s, 3H, $-OCH_3$), 4.59 (t, ^3J = 4.4 Hz, 2H, $-OCH_2CH_2$), 4.69 (s, 2H, $-OCH_2CO_2{}^t$Bu), 4.74 (s, 2H, $-OCH_2CO_2{}^t$Bu), 4.87 (s, 2H, $-OCH_2CO_2{}^t$Bu), 4.60 (t, ^3J = 4.3 Hz, 2H, $-OCH_2CH_2$), 7.26−7.81 (m, 16H, *p*-ArH, *m*-ArH, and *o*-ArH), 8.73 (d, ^2J = 4.8 Hz, 4H, βH-pyr), 8.81 (d, ^2J = 4.5 Hz, 4H, βH-pyr) ppm. ^{13}C NMR (100.4 MHz, $CDCl_3$): δ = 28.16 (9C, $-C(CH_3)_3$), 53.42, 53.94 (1C, $-OCH_3$), 64.99, 65.47 (1C, $-OCH_2CH_2$), 65.60, 65.74 (1C, $-OCH_2CH_2$), 67.07 (3C, $-CH_2CO_2-{}^t$Bu), 70.72 (2C, $C_{60}-sp^3$-C), 82.40 (2C, $-C(CH_3)_3$), 82.45 (1c, $-C(CH_3)_3$), 114.48, 114.90 (4C, *o*-ArC), 119.50, 119.79, 120.26, 120.75 (8C, *meso*-C), 123.45, 127.68, 128.29 (16C, *p*-ArC and *m*-ArC), ca. 131.20 (8C, 8C, βC-pyr), 137.35, 138. 93 (4C, *o*-ArC), 140.28, 140.85, 140.92, 141.09, 141.33, 141.40, 141.71, 142.21, 142.35, 142.77, 142.98, 143.10, 143.42, 143.53, 143.68, 143.82, 143.89, 143.97, 144.03, 144.24, 144.39, 144.49 (62C, $C_{60}-sp^2$-C, *ipso*-C), 156.10, 156.23, 156.33, 156.60 (11C, α-C and ArCO), 163.29, 163.63 (3C, $-\underline{C}O_2CH_2CO_2$, $-CO_2CH_2\underline{C}O_2$), 167.77, 167.94 (3C, $-CO_2-{}^t$Bu) ppm. IR (KBr): ν = 2978, 2155, 1711, 1644, 1653, 1388, 1365, 1290, 1250, 1154, 1109, 1032, 991, 944, 849, 795, 752 cm^{-1}. UV/vis (CH_2Cl_2): λ_{max} = 258, 328, 422, 517, 551, 591, 648 nm. MS (FAB, NBA): *m*/*z* = 1884 $[M]^+$, 1827, 1715 $[M - 3\times{}^t\text{Bu}]^+$, 1670, 1489, 1417, 1065. Anal. Calcd for $C_{128}H_{66}N_4O_{14}$ (1883.91) × EtOAc: C, 80.40; H, 3.78; N, 2.84; O, 12.98. Found: C, 77.86; H, 3.66; N, 3.01.

18. In a dry 250 mL flask with addition funnel were dissolved 400 mg (0.81 mmol) of **16** and 1.67 g (8.10 mmol, 10.0 equiv) of 9,10-dimethylanthracene in 100 mL of dry toluene under argon. The reaction mixture was stirred for 3 h at room temperature without exposure to light. 5.01 g (8.10 mmol, 10.0 equiv) of **17** and 2.68 g (8.10 mmol, 10.0 equiv) of CBr_4 were subsequently added. A solution of 2.42 mL (16.20 mmol, 20.0 equiv) of DBU in 50 mL of dry toluene was added slowly and dropwise. The reaction mixture was then stirred for 102 h at room temperature. Purification of **18** was carried out by flash chromatography (silica, CH_2Cl_2/EtOAc 9:1) with subsequent HPLC separation (nucleosil, CH_2Cl_2). The solvent was removed in vacuo, and the product was obtained as red brown solid in 11.2% yield. ^{1}H NMR (400 MHz, room temperature, CD_2Cl_2): δ = −2.79 (br, 2H, −NH), 0.88 (t, ^3J = 7.2 Hz, 15H, $-CH_2CH_3$), 0.98−1.56 (m, 300H, $-CH_2-$), 1.36 (q, ^3J = 7.1 Hz, 20H, $-CH_2CH_2CH_2COO-$), 1.45 (s, 9H, $-COOC(CH_3)_3$), 3.86 (br, 3H, $-OCCH_3$), 4.20−4.44 (br, 20H, $-C\underline{H}_2COO-$ and $-OOCC\underline{H}_2$), 4.70 (br, 4H, $-OCH_2-$), 7.28−7.94 (m, 16H, *p*-ArH, *m*-ArH, and *o*-ArH), 8.88 (m, 8H, βH-pyr) ppm. ^{13}C NMR (100.4 MHz, room temperature, CD_2Cl_2): δ = 14.31 (5C, $-CH_2CH_3$), 23.16 (5C, $-CH_2CH_3$), 26.27 (3C, $-COOC(CH_3)_3$), 28.15 (6C, $-COOC(CH_3)_3$), 28.84, 29.22, 29.78, 29.84, 30.11, 30.19, 32.21 (150C, $-CH_2-$), 66.26 (5C, $-OCH_2-$), 66.57 (3C, $-OCH_2CO-$), 68.85 (5C, $-CH_2CO-$), 72.01 (10C, $C_{60}-sp^3C$), 81.30 (3C, $-COOC(CH_3)_3$), 114.56 (1C, *o*-Ar*C*), 118.88 (4C, *meso*-*C*), 121.72 (1C, *p*-ArC), 126.53, 128.04 (3C, *o*-ArC), 129.99 (4C, *m*-ArC), 131.84 (8C, βC-pyr), 132.44 (3C, *p*-ArC), 142.06 (24C, $C_{60}-sp^2C$), 142.14 (1C, *ipso*-C), 143.99 (3C, *ipso*-C), 146.31 (24C, $C_{60}-sp^2C$), 156.82 (4C, *m*-ArCO−), 163.79 (2C, $-COOC(CH_3)_3$), 164.74 (1C, $-COOC(CH_3)_3$), 168.07 (2C, −CO−), 168.25 (10C, −CO−) ppm. IR (KBr): ν = 3323, 3034, 2930, 2853, 1729, 1709, 1625, 1575, 1538, 1474, 1440, 1407, 1312, 1272, 1243, 1178, 1154, 1089, 1069, 1031, 1001, 965, 892, 878, 846, 803, 730, 699, 658 cm^{-1}. UV/vis (CH_2Cl_2): λ_{max} = 400, 417, 514, 548, 589, 644 nm. MS (FAB, NBA): *m*/*z* = 4920 $[M]^+$. Anal. Calcd for $C_{323}H_{436}N_4O_{34}$ (4918.92) × C_7H_8 × EtOAc: C, 78.67; H, 8.93; N, 1.10; O, 11.30. Found: C, 76.32; H, 7.78; N, 1.44.

19. Compound **18** (100 mg, 20.1 μmol) and 10 mg (40.0 μmol) of zincacetate dihydrate in dried THF (40 mL) were stirred for 14 h under reflux in an argon atmosphere. The flash chromatographic purification of the metalated porphyrin was carried out with silica and dichloromethane/ethylacetate as eluents in a ratio of 1:1. Afterward, the polarity of the eluents was increased. After evaporation of the concentrated organic phases, the product was obtained as a red solid in quantitative yield. ^{1}H NMR (400 MHz, room temperature, CD_2Cl_2): δ = 0.90 (t, ^3J = 7.1 Hz, 15H, $-CH_2CH_3$), 1.01−1.52 (m, 300H, $-CH_2-$), 1.40 (q, ^3J = 7.1 Hz, 20H, $-CH_2CH_2CH_2COO-$), 1.44 (s, 9H, $-COOC(CH_3)_3$), 3.86 (br, 3H, $-OOCCH_3$), 4.24−4.46 (br, 20H, $-C\underline{H}_2COO-$ and $-OOCC\underline{H}_2$), 4.69 (br, 4H, $-OCH_2-$), 7.32−7.88 (m, 16H, *p*-ArH, *m*-ArH, and *o*-ArH), 9.00 (m, 8H, βH-pyr) ppm. ^{13}C NMR (100.4 MHz, room temperature, CD_2Cl_2): δ = 14.29 (5C, $-CH_2CH_3$), 23.11 (5C, $-CH_2CH_3$), 26.31 (3C, $-COOC(CH_3)_3$), 28.19 (6C, $-COOC(CH_3)_3$), 29.00, 29.35, 29.71, 29.79, 29.86, 30.15, 32.35 (150C, $-CH_2-$), 66.29 (5C, $-OCH_2-$), 66.52 (3C, $-OCH_2CO-$), 67.46 (5C, $-CH_2CO-$), 70.10 (10C, $C_{60}-sp^3C$), 82.50 (3C, $-COOC(CH_3)_3$), 114.39 (1C, *o*-ArC), 120.99 (4C, *meso*-C), 121.36 (1C, *p*-ArC), 127.86, 128.65 (3C, *o*-ArC), 129.13 (4C, *m*-ArC), 131.29, 132.34 (8C, βC-pyr), 132.84 (3C, *p*-ArC), 141.43 (24C, $C_{60}-sp^2C$), 142.54 (1C, *ipso*-C), 144.62 (3C, *ipso*-C), 146.06 (24C, $C_{60}-sp^2C$), 150.50 (8C, αC-pyr), 156.81 (4C, *m*-ArCO−), 164.06 (2C, $-COOC(CH_3)_3$), 164.36 (1C, $-COOC(CH_3)_3$), 167.89 (2C, −CO−), 168.25 (10C, −CO−) ppm. IR (KBr): ν = 2150, 1733, 1649, 1520, 1397, 1393, 1301, 1288, 1249, 1134, 1100, 1065, 994, 952, 847, 792, 750, 701, 660 cm^{-1}. UV/vis (CH_2Cl_2): λ_{max} = 400, 424, 556 nm. MS (FAB, NBA): *m*/*z* = 4984 $[M + H]^+$. Anal. Calcd for $C_{323}H_{434}N_4O_{34}Zn$ (4982.32) × $2C_7H_8$ × EtOAc: C, 77.94; H, 8.79; N, 1.07; O, 10.96. Found: C, 77.65; H, 9.01; N, 1.35.

Acknowledgment. This work was supported by the Cluster of Excellence "Engineering of Advanced Materials", by a Grant-in-Aid for Scientific Research Priority Area (19205019 and 19750034) from the Ministry of Education, Culture, Sports, Science and Technology, Japan, and by the Deutsche Forschungsgemeinschaft through SFB583.

JA900675T